# Reproducing the CMB power spectrum

C. Villandseie[1]

Institute of Theoretical Astrophysics, University of Oslo, 0315 Oslo, Norway
e-mail: chrv@uio.no
Link to Github repository: https://github.com/chrvill/AST5220

June 2022

**ABSTRACT**

We describe how one can compute the power spectrum of the cosmic microwave background from scratch. All the physics needed is explained, and there is a focus on the numerical issues that likely will arise when writing such a program. The paper is divided into four milestones, each of which deals with different aspects of the process on the way to computing the power spectrum. The focus in this paper is on the $\Lambda$CDM model, but the physics and algorithms can very easily be used for other cosmological models. We neglect neutrinos and polarization here, which does cause discrepancies relative to observations. But the main goal is to gain an understanding for how one can compute the CMB power spectrum from scratch, and the qualitative behavior of the model introduced here fulfills that wish. When dealing with perturbations on top of the smooth background universe we work in linear perturbation theory, which makes the physics far simpler. And throughout we assume a flat universe. The computed power spectrum does deviate from the power spectrum inferred from Planck 2018 observations of the CMB, which is caused by our omission of neutrinos and polarization.

## 1. Introduction

The possibility of observing the cosmic microwave background (CMB) and its anisotropies quickly transformed cosmology into a proper field of science. In the time since the Cosmic Background Explorer (COBE) first observed the anisotropies in the early 90's the measurements have become increasingly precise. The Wilkinson Microwave Anisotropy Probe (WMAP) and Planck satellite after it gained higher and higher resolutions of the CMB map. This allowed for determining the CMB power spectrum on smaller angular scales. As the observations have become increasingly precise the need to compute theoretical predictions for the power spectrum has also become increasingly important. There now exist many programs for computing the power spectrum, like CMBFAST and CAMB. These can be used to fit the cosmological parameters to observations, and thus determine the best cosmological model. But these programs hide most of the physics from view. Our goal in this paper is to construct a program, similar to CMBFAST and CAMB, that can compute the CMB power spectrum for a given cosmological model. This includes discussing the physics at each step in the process. In this way the physics (and assumptions) going into predicting the CMB power spectrum should become clear. We will introduce all the parts needed to compute the power spectrum from scratch, along with algorithms that will help with the numerical aspects of the computations. In this model we will neglect neutrinos and polarization. This will of course cause a discrepancy between our results and those produced by CMB-FAST, for instance. But the qualitative understanding can still be gained. And since this work is mainly done to get an understanding of the physics this sacrifice in quantitative accuracy is not critical.

The paper is divided into four milestones, where each one handles a different aspect of the physics needed to compute the power spectrum. Milestone I deals with the background cosmology in a smooth universe, computing expansion rate, conformal time etc. as functions of the time variable, $x = \log a$ ($a$ being the scale factor of the universe), we will be using throughout. Milestone II tackles the recombination history of the universe. So here we compute the electron fraction and optical depth as functions of time. This is used to study when recombination occurs in our model. Milestone III introduces perturbations to the densities and velocities of the different species in the universe. We then present the differential equations governing their evolution, and solve for this evolution. Assuming the perturbations are small allows us to work in linear perturbation theory. That is a great simplification, because when transforming the evolution equations into Fourier space the fact that we neglect higher orders in the perturbations means that all the different Fourier modes are independent. So we can solve for each Fourier mode independently. Milestone IV then finally uses all of the previous results to compute the CMB power spectrum and the matter power spectrum. Here we also explore how the CMB power spectrum changes when changing the cosmological parameters. All the milestones are further divided up into three parts: theory, implementation details, and results. The theory section deals with the physics needed to compute the relevant quantities, and the equations we need. Here we also discuss assumptions that are made to simplify calculations. The implementation details section discusses the algorithms used, and how these are adapted in the code to produce numerically stable and accurate results. The results section then presents the computed quantities and discusses their implications and how these make sense given the physics. This paper is inspired by Callin (2006) and Winther (2021). We will for the most part not perform derivations here (in the few cases when there are derivations, these are given in the appendices), but these can be found mainly in Winther (2021) or Dodelson (2011).

## 2. Milestone I

In this milestone the goal is to solve the Friedmann equations numerically in order to obtain information about the background cosmology of the homogeneous and isotropic universe.

### 2.1. Theory

The line element in a flat, homogeneous and isotropic universe is given by

$$ds^2 = -c^2 dt^2 + a^2(t)\left[dr^2 + r^2\left(d\theta^2 + \sin^2\theta d\phi^2\right)\right], \tag{1}$$

where $c$ is the speed of light, and $r, \theta, \phi$ are the coordinates in a spherical coordinate system. $a$ is the scale factor of the universe.

The first Friedmann equation can be written as

$$H = H_0 \sqrt{\left(\Omega_{b0} + \Omega_{\text{CDM0}}\right)a^{-3} + \left(\Omega_{\gamma 0} + \Omega_{\nu 0}\right)a^{-4} + \Omega_{k0}a^{-2} + \Omega_{\Lambda 0}}, \tag{2}$$

with $H = \frac{\dot{a}}{a}$ being the Hubble parameter, $H_0$ the Hubble parameter today, and $\Omega_{b0}, \Omega_{\text{CDM0}}, \Omega_{\gamma 0}, \Omega_{\nu 0}$ and $\Omega_{\Lambda 0}$ being the density parameters today of baryons, dark matter, photons, neutrinos and dark energy, respectively. $\Omega_{k0} = -\frac{kc^2}{H_0^2}$ is the curvature density parameter, where $k$ denotes the curvature of space. The subscript 0 will throughout this paper refer to the value of a certain quantity today. The density parameter of a component $i$ is given by

$$\Omega_{i0} = \frac{\rho_{i0}}{\rho_{\text{crit},0}}, \quad \rho_{\text{crit},0} = \frac{3H_0^2}{8\pi G}, \tag{3}$$

with $G$ being Newton's gravitational constant. The densities of the components we will consider depend on the scale factor in the following ways:

$$\rho_{\text{CDM}} = \rho_{\text{CDM},0}a^{-3} \tag{4}$$
$$\rho_b = \rho_{b,0}a^{-3} \tag{5}$$
$$\rho_\gamma = \rho_{\gamma,0}a^{-4} \tag{6}$$
$$\rho_\nu = \rho_{\nu,0}a^{-4} \tag{7}$$
$$\rho_\Lambda = \rho_{\Lambda,0}. \tag{8}$$

The density parameter of radiation and neutrinos today can be expressed as functions of the temperature of the CMB today. The relations are

$$\Omega_{\gamma 0} = 2 \cdot \frac{\pi^2}{30} \frac{(k_b T_{\text{CMB0}})^4}{\hbar^3 c^5} \cdot \frac{8\pi G}{3H_0^2} \tag{9}$$

$$\Omega_{\nu 0} = N_{\text{eff}} \cdot \frac{7}{8} \cdot \left(\frac{4}{11}\right)^{4/3} \Omega_{\gamma 0}, \tag{10}$$

where $k_b$ is Boltzmann's constant, and $\hbar$ is the reduced Planck's constant. $T_{\text{CMB},0}$ is the temperature of the CMB today, and $N_{\text{eff}}$ is the effective number of massless neutrinos.

Since the scale factor will span many orders of magnitude it will be useful to introduce a quantity $x \equiv \log a$. It is also useful to introduce the conformal time, $\eta$, defined by

$$\frac{d\eta}{dt} = \frac{c}{a}, \tag{11}$$

which can be rewritten into

$$\frac{d\eta}{dx} = \frac{c}{\mathcal{H}}, \tag{12}$$

with $\mathcal{H} \equiv aH$. In Appendix A.4 we derive the analytical expression $\eta(x) = \frac{c}{\mathcal{H}(x)}$ in the radiation dominated regime. And this can be used to initialize the differential equation by choosing an early $x_{\text{start}}$ at the beginning, and setting $\eta(x_{\text{start}}) = \frac{c}{\mathcal{H}(x_{\text{start}})}$.

Similarly we can write a differential equation for $t$;

$$\frac{dt}{dx} = \frac{1}{H}. \tag{13}$$

Appendix A.4 also includes a derivation of $t(x) = \frac{1}{2H(x)}$ during radiation domination. So we have an initial condition for this differential equation as well.

Because we will be interested in measuring distances in the universe we will also introduce the comoving distance, $\chi = \eta_0 - \eta$. The radial comoving coordinate is then given by

$$r = \begin{cases} \chi \cdot \frac{\sin\left(\sqrt{|\Omega_{k0}|}H_0\chi/c\right)}{\left(\sqrt{|\Omega_{k0}|}H_0\chi/c\right)} & \Omega_{k0} < 0 \\ \chi & \Omega_{k0} = 0 \\ \chi \cdot \frac{\sinh\left(\sqrt{|\Omega_{k0}|}H_0\chi/c\right)}{\left(\sqrt{|\Omega_{k0}|}H_0\chi/c\right)} & \Omega_{k0} > 0 \end{cases} \tag{14}$$

The distances we will be interested in here are the angular diameter distance, $d_A$, and the luminosity distance, $d_L$. These can then be defined in terms of $r$:

$$d_A = ar \tag{15}$$
$$d_L = \frac{r}{a} \tag{16}$$

All of this is taken from Winther (2022a).

### 2.2. Implementation details

To avoid complications in later milestones we will throughout all the milestones set $N_{\text{eff}} = 0$ and $\Omega_{k0} = 0$. This means we are working with a flat universe without neutrinos. The input parameters to the code solving the background cosmology are thus (Planck 2018 data):

$$h = 0.67, \tag{17}$$
$$T_{\text{CMB0}} = 2.7255\,K, \tag{18}$$
$$N_{\text{eff}} = 0, \tag{19}$$
$$\Omega_{b0} = 0.05, \tag{20}$$
$$\Omega_{\text{CDM0}} = 0.267, \tag{21}$$
$$\Omega_{k0} = 0, \tag{22}$$

and the other parameters that are needed, like $\Omega_{\Lambda0}$, $\Omega_{\gamma0}$ and $H_0$ are derived from these ($\Omega_{\nu0}$ as well, but it will always be zero here). $H_0$ and $\Omega_{\Lambda0}$ are given by

$$H_0 = 100\frac{\text{km/s}}{\text{Mpc}} \cdot h \tag{23}$$
$$\Omega_{\Lambda0} = 1 - (\Omega_{k0} + \Omega_{b0} + \Omega_{\text{CDM0}} + \Omega_{\gamma0} + \Omega_{\nu0}). \tag{24}$$

$\Omega_{\gamma0}$ is then calculated using equation (9).

In the code we create an array of $x$-values in a certain range, $[x_{\min}, x_{\max}]$, and calculate all the relevant quantities; $H(x), \mathcal{H}(x), \frac{dH}{dx}, \frac{d\mathcal{H}}{dx}, \frac{d^2H}{dx^2}, \frac{d^2\mathcal{H}}{dx^2}, \Omega_b(x), \Omega_{\text{CDM}}(x)$ and $\Omega_\gamma(x)$ for each value of $x$. This we can do because these are all explicit functions of $a$, and $a = e^x$ (the expressions for the derivatives of $H$ and $\mathcal{H}$ with respect to $x$ are derived in Appendix A.1).

In order to get $\eta(x)$ and $t(x)$ we need to solve the differential equations defined in (12) and (13). For this we use the Runge-Kutta 4 ODE solver to solve the ODEs between $x_{\min}$ and $x_{\max}$. Then we create a cubic spline that interpolates between the values of $x$ for which the ODEs were solved.

### 2.3. Results

We considered 10 000 linearly spaced $x$-values in the range $[-20, 5]$ and calculated $H(x), \mathcal{H}(x)$ etc. for all these $x$-values. The differential equations (12) and (13) are then solved for these same $x$-values. The results from the differential equations are then splined. In Appendix A.5 we derive the expressions for the redshift at which matter-radiation equality, matter-dark energy equality and the start of accelerated expansion occur. This can then be computed for the parameters used in the code. These times are given in Table 1, in terms of redshift, $x$ and time.

| Event | Redshift $z$ | $x$ | Time $t$ [Gyr] |
|---|---|---|---|
| Matter-rad. eq. | 5750 | -8.66 | $2.3 \cdot 10^{-5}$ |
| Matter-$\Lambda$ eq | 0.29 | -0.26 | 10.4 |
| Acc. begins | 0.63 | -0.49 | 7.8 |

**Table 1.** Points at which matter-radiation equality, matter-dark energy equality and start of accelerated expansion occur. These are given in terms of redshift, time and $x$.

Matter-radiation equality is generally accepted to have occurred at around $z \sim 3000$, which is at odds with the result in Table 1. But in these calculations we have neglected the contribution to the radiation energy density from neutrinos. If we include neutrinos by setting $N_{\text{eff}} = 3.046$, then we get $z \approx 3400$,

which is much closer. Matter-dark energy equality and start of acceleration happen quite close to one another. This is because dark energy causes the accelerated expansion, so the expansion can only accelerate when the dark energy contribution is significant. The three aforementioned events are marked with dashed vertical lines in all the following plots in the background cosmology section.

Figures 1 and 2 show the evolution of $H(x)$ and $\mathcal{H}(x)$, respectively, as functions of $x$. The $x$-range in the plot has been limited to $x \in [-12, 5]$ in order to be able to see details, and the $y$-axes are logarithmic. In all the following plots the leftmost vertical dashed line represents the value of $x$ for which we have matter-radiation equality, the line in the middle is for the start of accelerated expansion, and the rightmost line is for matter-dark energy equality.
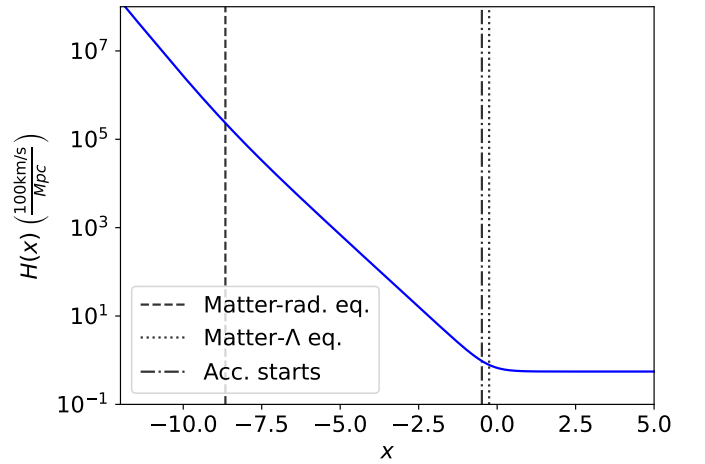


**Fig. 1.** $H(x)$ for $x \in [-12, 5]$. The $y$-axis is logarithmic and shows $H(x)$ in units of $\frac{100\,\text{km/s}}{\text{Mpc}}$. The dashed vertical lines show the values of $x$ for which matter-radiation equality, start of accelerated expansion, and matter-dark energy equality occurred, respectively.
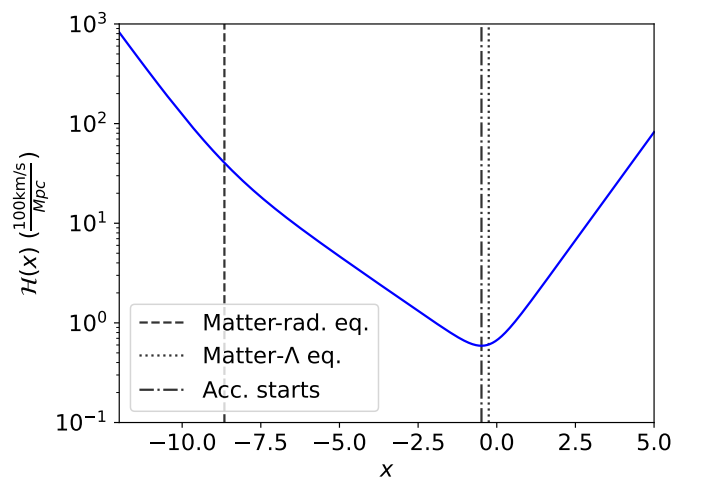


**Fig. 2.** $\mathcal{H}(x)$ for $x \in [-12, 5]$. The $y$-axis is logarithmic and shows $\mathcal{H}(x)$ in units of $\frac{100\,\text{km/s}}{\text{Mpc}}$. The dashed vertical lines again show the values of $x$ for which matter-radiation equality, start of accelerated expansion, and matter-dark energy equality occurred, respectively.

$H(x)$ decreases with $x$ (and thus also with the scale factor, $a$, and time, $t$) during the radiation and matter dominated periods. It decreases most rapidly during radiation domination, the explanation for which is straight forward; during radiation domination $H(x) = H_0 \sqrt{\Omega_{r0}e^{-4x}} \sim e^{-2x}$, while during matter domination $H(x) = \sqrt{\Omega_{m0}e^{-3x}} \sim e^{-3/2x}$. During dark energy domination $\Omega \approx$ constant, which is why $H(x)$ is flat in this period. During this period the universe expands approximately exponentially, and with such an expansion the Hubble parameter is constant.

The shape of $\mathcal{H}(x)$ can be explained in a very similar way. During radiation domination $\mathcal{H} \sim a \cdot a^{-2} = e^{-x}$, during matter domination we have $\mathcal{H}(x) \sim a \cdot a^{-3/2} = e^{-1/2x}$, and during dark energy domination $\mathcal{H}(x) \sim a = e^x$. This agrees with the fact that the slope of $\mathcal{H}(x)$ during matter domination is smaller than during the other periods, and that the slopes (in absolute value) during radiation and dark energy domination are the same. $\mathcal{H}$ can be written as $\mathcal{H} = \dot{a}$, so it represents the rate of change of the scale factor. This means that the expansion is slowing down during both radiation and matter domination, but the slowing down is quicker in the radiation dominated era. And during the dark energy dominated era the scale factor increases exponentially.

Figures 3 and 4 show $\frac{1}{\mathcal{H}}\frac{d\mathcal{H}}{dx}$ and $\frac{1}{\mathcal{H}}\frac{d^2\mathcal{H}}{dx^2}$ plotted as functions of $x$. The $x$-range is now restricted to $x \in [-15, 5]$, again in order to see details.
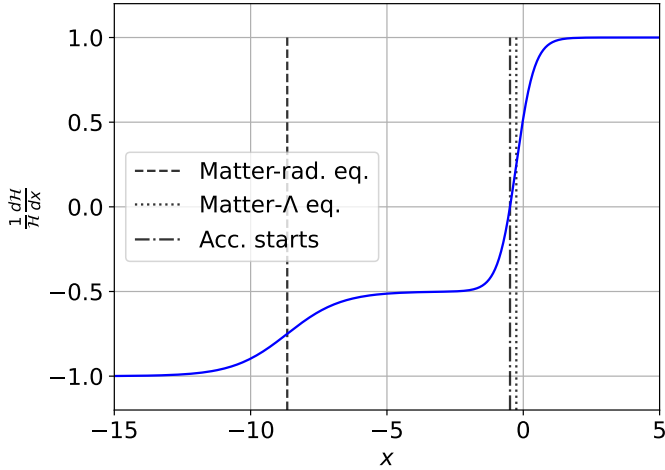


**Fig. 3.** $\frac{1}{\mathcal{H}(x)}\frac{d\mathcal{H}}{dx}$ for $x \in [-15, 5]$. The $y$-axis is dimensionless. The dashed vertical lines again show the values of $x$ for which matter-radiation equality, start of accelerated expansion, and matter-dark energy equality occurred, respectively.
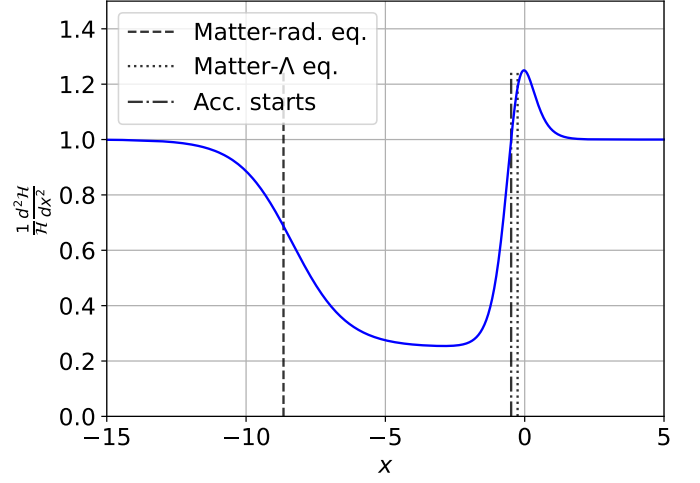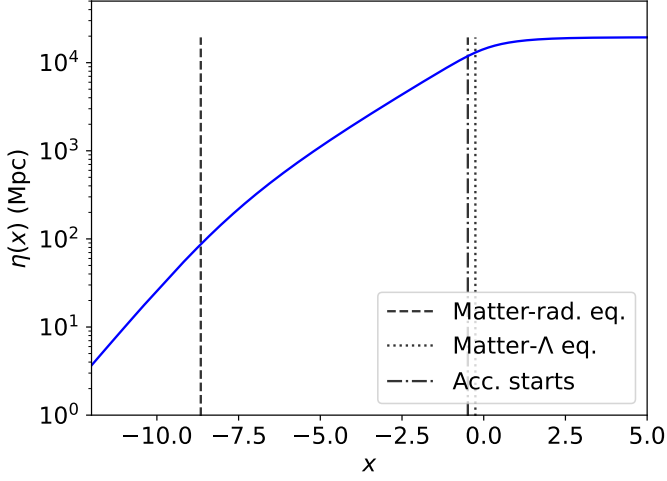


**Fig. 4.** $\frac{1}{\mathcal{H}(x)}\frac{d^2\mathcal{H}}{dx^2}$ for $x \in [-15, 5]$. The $y$-axis is dimensionless. The dashed vertical lines again show the values of $x$ for which matter-radiation equality, start of accelerated expansion, and matter-dark energy equality occurred, respectively.

In Appendices A.2 and A.3 we derive the values of $\frac{1}{\mathcal{H}}\frac{d\mathcal{H}}{dx}$ and $\frac{1}{\mathcal{H}}\frac{d^2\mathcal{H}}{dx^2}$ during matter, radiation and dark energy domination. We found that $\frac{1}{\mathcal{H}}\frac{d\mathcal{H}}{dx}$ has a value of $-1, \frac{1}{2}$ and $1$ during radiation, matter and dark energy domination, respectively. This is in agreement with the numerical results shown in Figure 3. And we found that $\frac{1}{\mathcal{H}}\frac{d^2\mathcal{H}}{dx^2}$ has a value of $1, \frac{1}{4}$ and $1$ during radiation, matter and dark energy domination, respectively. This again agrees with the numerical results.

The point at which $\frac{1}{\mathcal{H}}\frac{d\mathcal{H}}{dx}$ crosses zero is of interest. The plot shows that it happens when the expansion of the universe starts accelerating, and that is not a coincidence. $\mathcal{H} = \dot{a}$, so the expression can be written as

$$\frac{1}{\mathcal{H}}\frac{d\mathcal{H}}{dx} = \frac{1}{\dot{a}}\frac{da}{dx}\frac{dt}{da}\frac{d\dot{a}}{dt} = \frac{a\ddot{a}}{\dot{a}^2}. \tag{25}$$

So when the expansion goes from slowing down, meaning $\ddot{a} < 0$, to accelerating, meaning $\ddot{a} > 0$, then $\frac{1}{\mathcal{H}}\frac{d\mathcal{H}}{dx} = 0$. A similar intuition is not as easy to draw from $\frac{1}{\mathcal{H}}\frac{d^2\mathcal{H}}{dx^2}$, since it involves $\dddot{a}$. Figures 5, 6 and 7 show $\eta(x)$, $\frac{\eta(x)\mathcal{H}}{c}$ and $t(x)$, respectively. The first and last plots have logarithmic $y$-axes, the first one in Mpc, and the last one in Gyr. The plot of $\eta$ is restricted to $x \in [-12, 5]$, $\frac{\eta\mathcal{H}}{c}$ is restricted to $x \in [-15, 0]$, and $t$ is restricted to $x \in [-15, 5]$. All of this is to be able to see details.

**Fig. 5.** $\eta(x)$ for $x \in [-12, 5]$. The $y$-axis is logarithmic, and shows $\eta(x)$ in units of Mpc. The dashed vertical lines again show the values of $x$ for which matter-radiation equality, start of accelerated expansion, and matter-dark energy equality occurred, respectively.
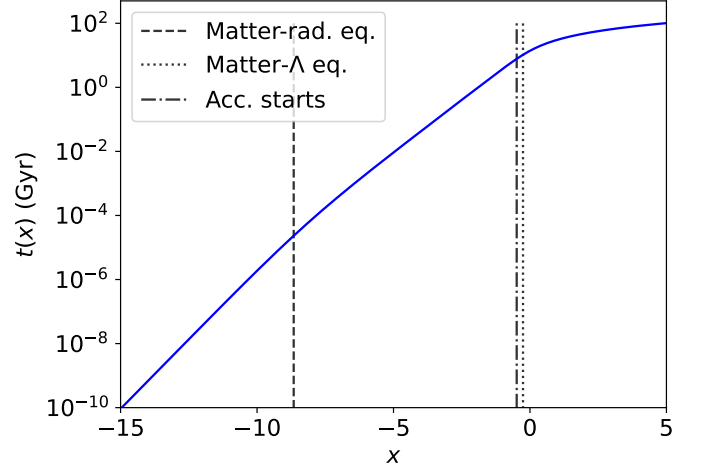


**Fig. 7.** $t(x)$ for $x \in [-15, 5]$. The $y$-axis is logarithmic, and shows $t(x)$ in units of Gyr. The dashed vertical lines again show the values of $x$ for which matter-radiation equality, start of accelerated expansion, and matter-dark energy equality occurred, respectively.
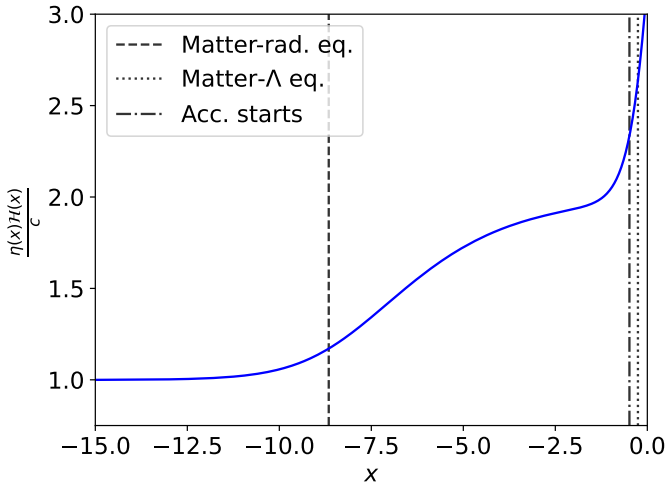


**Fig. 6.** $\frac{\eta(x)\mathcal{H}(x)}{c}$ for $x \in [-15, 0]$. The $y$-axis is logarithmic, and the $y$-axis is dimensionless. The dashed vertical lines again show the values of $x$ for which matter-radiation equality, start of accelerated expansion, and matter-dark energy equality occurred, respectively.

Figure 5 and 7 are very similar. The reason is that $\eta(x)$ represents the comoving distance to the particle horizon, while $t(x)$ represents the age of the universe. These two concepts are of course very closely related. ($\eta = \int_0^t \frac{cdt'}{a}$, where $t$ is the age of the universe). $t$ increases faster as a function of $x$ during radiation than during matter domination, which agrees with the analytical expressions $a \propto t^{1/2}$ during radiation domination and $a \propto t^{2/3}$ during matter domination. During dark energy domination both $\eta(x)$ and $t(x)$ increase very slowly with $x$. For $t$ this is because during that era $a \propto e^{Ht}$. $\eta(x)$ approaches a constant in that period. This is because $\mathcal{H}$ increases during dark energy domination, see Figure 2. And $\frac{d\eta}{dx} = \frac{c}{\mathcal{H}}$, so $\eta$ decreases with time during dark energy domination. This is to say that the particle horizon approaches a constant. Objects at comoving distances smaller than $\eta$ will have had time to interact with us, wile objects farther away have not. Since $\eta$ approaches a constant there will be a smallest comoving distance such that objects at that distance will never have had time to interact with us. This is due to the exponential expansion in $a$ during dark energy domination.

From Appendix A.4 we know that $\eta(x) = \frac{c}{\mathcal{H}}$ during radiation domination. So the ratio $\frac{\eta \mathcal{H}}{c}$ should be equal to 1 during that epoch. Figure 6 shows that this is indeed the case, so the computed and analytical results agree. When the scale factors evolves according to a power law the conformal time can be written as $\eta(x) = \frac{A}{\mathcal{H}}$, for some constant $A$. So $\frac{\eta \mathcal{H}}{c}$ is essentially telling us the proportionality constant relating $\eta$ to $\mathcal{H}$. Figure 6 shows that this proportionality constant evolves over time, and is different during radiation domination and matter domination, as it should be.

Figure 8 shows the density parameters $\Omega_m = \Omega_b + \Omega_{CDM}$, $\Omega_r = \Omega_\gamma + \Omega_\nu$ and $\Omega_\Lambda$ plotted as functions of $x$.
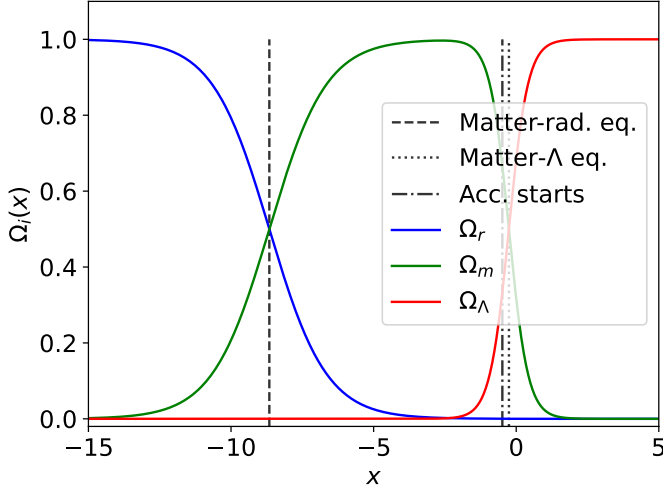
**Fig. 8.** $\Omega_i(x)$ for $x \in [-15, 5]$ for $i = $ r, $i = $ m and $i = \Lambda$. Here $\Omega_m$ corresponds to $\Omega_b + \Omega_{CDM}$ and $\Omega_r$ corresponds to $\Omega_\gamma + \Omega_\nu$ (at least in general. Here $\Omega_\nu$ is zero at all times). The $y$-axis is dimensionless. The dashed vertical lines again show the values of $x$ for which matter-radiation equality, start of accelerated expansion, and matter-dark energy equality occurred, respectively.

The dashed vertical line representing matter-radiation equality falls at the intersection of $\Omega_m(x)$ with $\Omega_r(x)$, which it should. The same holds for matter-dark energy equality. $\Omega_r$ dominates during early times, $\Omega_m$ dominates between matter-radiation and matter-dark energy equality, and $\Omega_\Lambda$ dominates after matter-dark energy equality. This is just as expected. The sum of the density parameters does not exceed 1 either, again as expected.

Figure 9 shows the luminosity distance as a function of redshift for the observational data and the computed luminosity distance as function of redshift. The $y$-axis is in Gpc.
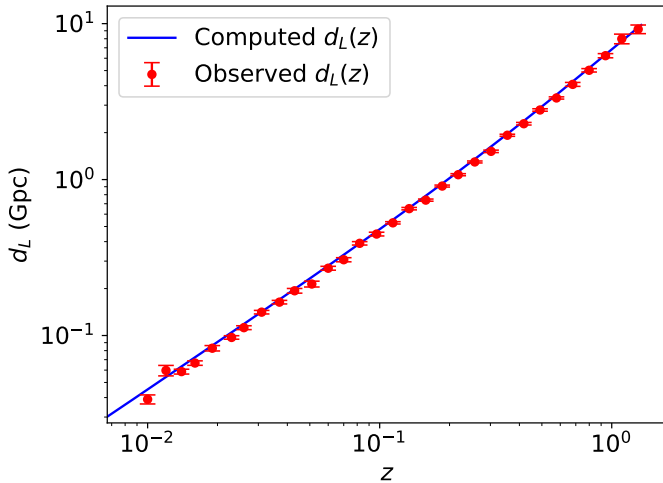


**Fig. 9.** Luminosity distance, $d_L$, as a function of redshift calculated numerically and inferred from observations. The blue curve shows the numerically computed luminosity distances, while the red points show the data points from observations. The $y$-axis is in units of Gpc. Both axes are logarithmic.

This seems to fit quite well, but plotting this without logscale tells a different story. Figure 10
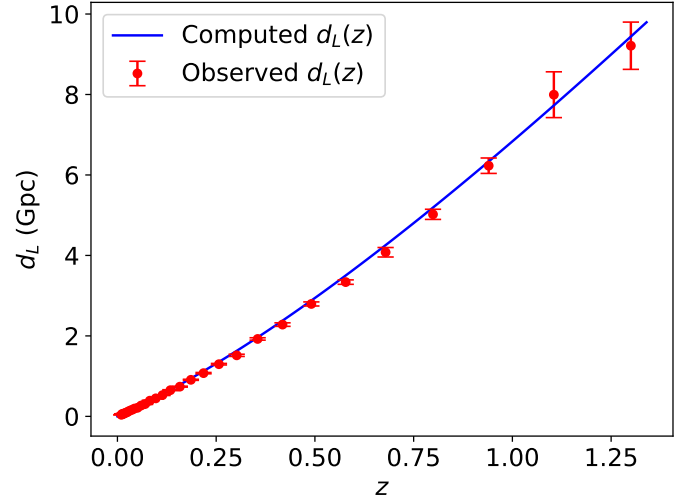


**Fig. 10.** Luminosity distance, $d_L$, as a function of redshift calculated numerically and inferred from observations. The blue curve shows the numerically computed luminosity distances, while the red points show the data points from observations. The $y$-axis is in units of Gpc.

We see that for $z > 0.25$ our predicted curve falls outside the error bars of most of the data points. This is the so-called Hubble tension. Measurements of $H_0$ from stars and galaxies infer a value $H_0 \approx 73$ km/s Mpc$^{-1}$, while observations of the CMB favour $H_0 \approx 67$ km/s Mpc$^{-1}$ (see for example Valentino (2021)).

From the spline for $t(x)$ that we created we computed the age of the universe today, and got $t_0 \approx 13.86$ Gyr. This is close to the generally accepted value of around 13.8 Gyr. The same thing can be done for the spline of $\eta(x)$, giving $\eta_0 \approx 46.5$ Gly, corresponding to the radius of the observable universe today (for a flat universe, which we have assumed).

## 3. Milestone II

In order to compute the CMB power spectrum we will need to know the optical depth of the universe as a function of time. The reason for this is twofold: the expressions for the time derivatives of the perturbation variables that we will later introduce contain time derivatives of the optical depth. And after the CMB left the last scattering surface the photons had to travel through the universe and will have encountered some electrons along the way. So knowing the optical depth at all times is essential in order to predict the CMB power spectrum. Then we need to know the number density of electrons as a function of time. The goal in this milestone is to compute this number density of electrons, and using this we will calculate the optical depth at all times. This is done for the background universe, so we are still assuming a smooth universe.

### 3.1. Theory

The optical depth, $\tau$, represents the strength of the scattering in a medium (in general both absorption and scattering, but here

only scattering). As radiation travels through a medium the intensity will be reduced due to scattering, and this reduction can be quantified by the optical depth. If the initial intensity of the incoming radiation is $I_0$, then the outgoing intensity after travelling through a medium with optical depth $\tau$ is $I = I_0 e^{-\tau}$. The optical depth is also related to the probability of a photon being scattered, which is given by $1 - e^{-\tau}$. So the larger $\tau$ is, the closer the scattering probability is to 1.

Here we will only consider scattering off of free electrons, in which case the expression for the optical depth is

$$\tau = \int_\eta^{\eta_0} n_e \sigma_T a d\eta', \tag{26}$$

where $\sigma_T$ is the Thomson cross section for free electron scattering, and $n_e$ is the number density of free electrons. In principle we would also need to compute the contribution to the optical depth from free protons and hydrogen atoms etc. But the scattering cross section is inversely proportional to the square of the mass of the particle involved, so the scattering cross section due to free protons and hydrogen will be $\left(\frac{m_e}{m_p}\right)^2 \approx 10^{-6}$ times smaller than that of free electrons. $m_e$ and $m_p$ are the masses of the electron and proton respectively (mass of hydrogen is approximately the mass of the proton). The cross sections of proton and hydrogen scattering will thus be much smaller than for electrons, and thus these forms of scattering can safely be neglected.

We know from milestone I that

$$ad\eta = a\frac{c}{a}dt = c\frac{dt}{da}da = c\frac{dt}{da}\frac{da}{dx}dx = c\frac{1}{\dot{a}}adx = \frac{c}{H}dx,$$

so that

$$\tau = \int_x^0 \frac{c n_e \sigma_T}{H}dx. \tag{27}$$

This means that

$$\tau' = \frac{d\tau}{dx} = -\frac{c n_e \sigma_T}{H}, \tag{28}$$

which is the equation we will use to compute $\tau$ when we know $n_e$. The number density of free electrons can be found using the Boltzmann equation. When the interaction rate between photons and free electrons is much higher than the Hubble expansion rate, $H$, the Boltzmann equation can be approximated as the Saha equation, given by

$$\frac{X_e^2}{1 - X_e} = \frac{1}{n_b}\left(\frac{m_e k_B T_b}{2\pi\hbar^2}\right)^{3/2} e^{-\epsilon_0/(k_B T_b)}, \tag{29}$$

where $X_e = \frac{n_e}{n_H}$ is the free electron fraction, $n_b = \frac{\Omega_{b0}\rho_{c0}}{m_H a^3}$ is the number density of baryons, $T_b$ is the temperature of the baryons,

$\epsilon_0 \approx 13.6$ eV is the ionisation energy of hydrogen, $k_B$ is Boltzmann's constant and $\hbar$ is the reduced Planck constant. This equation assumes there is no helium in the universe. In this paper we will take helium into account, but for completeness we also give the expression needed for performing the computations without helium.

Computing $n_e$ boils down to finding $X_e$ and using that $n_e = X_e n_H$. So we need to solve (29), which is a simple quadratic equation. This can be rewritten as

$$X_e^2 + CX_e - C = 0, \tag{30}$$

where $C$ is the right hand side of (29). $C$ is a function of $x$ through $T_b$ and $n_b$, so needs to be solved for each value of $x$. Here we will assume the baryon temperature $T_b$ is equal to the photon temperature $T_{CMB}$ which just goes as $T_{CMB} = \frac{T_{CMB,0}}{a}$, where $T_{CMB,0}$ is the CMB temperature today. This is almost always true, but has a slight caveat. Before (and after) electrons and positrons annihilate the photon temperature decreases as $T_\gamma \propto a^{-1}$, but when they annihilate their energy is injected into the photons. So there is a slight increase in the photon temperature relative to the temperature without annihilation. This means our assumption $T_{CMB} = \frac{T_{CMB,0}}{a}$ will be valid all the way from electron/positron annihilation until today, but not before annihilation. This is not problematic, since recombination happens long after electron/positron annihilation (the latter happens when $T \sim$ Mev). The theory concerning electron and positron annihilation is explained in more detail in section 4.5 of Øystein Elgarøy (2021).

The baryon density can be computed using the formula defined above.

As mentioned we will be taking helium into account, so instead of the Saha equation (29) we will need the following three equations

$$n_e \frac{x_{He+}}{1 - x_{He+} - x_{He++}} = 2\left(\frac{m_e k_B T_b}{2\pi\hbar^2}\right)^{3/2} e^{-\chi_0/(k_B T_b)}, \tag{31}$$

$$n_e \frac{x_{He++}}{x_{He+}} = 4\left(\frac{m_e k_B T_b}{2\pi\hbar^2}\right)^{3/2} e^{-\chi_1/(k_B T_b)}, \tag{32}$$

$$n_e \frac{x_{H+}}{1 - x_{H+}} = \left(\frac{m_e k_B T_b}{2\pi\hbar^2}\right)^{3/2} e^{-\epsilon_0/(k_B T_b)}, \tag{33}$$

where $\chi_0 = 24.5874$ eV is the ionisation energy of He and $\chi_1 = 54.42279$ eV is the ionisation energy of He$^+$. Then

$$\frac{n_e}{n_b} = (2x_{He++} + x_{He+})\frac{Y_p}{4} + x_{H+}(1 - Y_p) \equiv f_e \implies X_e = \frac{f_e}{1 - Y_p} \tag{34}$$

where $Y_p$ is the mass fraction of helium. These expressions are taken from Winther (2022b).

When the interaction rate of photons and free electrons is not much higher than $H$ the gas falls out of thermal equilibrium with

the photons, so the equilibrium expressions (29), (31), (32) and (33) are not valid anymore. We will instead need the Peebles equation, which is

$$\frac{dX_e}{dx} = \frac{C_r(T_b)}{H} \left[ \beta(T_b)(1 - X_e) - n_H \alpha^{(2)}(T_b) X_e^2 \right],\qquad (35)$$

where

$$C_r(T_b) = \frac{\Lambda_{2s\to1s} + \Lambda_\alpha}{\Lambda_{2s\to1s} + \Lambda_\alpha + \beta^{(2)}(T_b)}, \quad \text{(dimensionless)},\qquad (36)$$

$$H, \quad \text{(dimension 1/s)}\qquad (37)$$

$$\Lambda_{2s\to1s} = 8.227\text{s}^{-1}, \quad \text{(dimension 1/s)}\qquad (38)$$

$$\Lambda_\alpha = H \frac{(3\epsilon_0)^3}{(8\pi)^2 \hbar^3 c^3 n_{1s}}, \quad \text{(dimension 1/s)}\qquad (39)$$

$$n_{1s} = (1 - X_e) n_H, \quad \text{(dimension 1/m}^3\text{)}\qquad (40)$$

$$n_H = (1 - Y_p) \frac{3 H_0^2 \Omega_{b0}}{8\pi G m_H a^3}, \quad \text{(dimension 1/m}^3\text{)}\qquad (41)$$

$$\beta^{(2)}(T_b) = \beta(T_b) e^{3\epsilon_0/(4k_B T_b)}, \quad \text{(dimension 1/s)}\qquad (42)$$

$$\beta(T_b) = \alpha^{(2)}(T_b) \left( \frac{m_e k_B T_b}{2\pi\hbar^2} \right)^{3/2} e^{-\epsilon_0/(k_B T_b)}, \quad \text{(dimension 1/s)}\qquad (43)$$

$$\alpha^{(2)}(T_b) = \frac{8\sigma_T c}{\sqrt{3\pi}} \sqrt{\frac{\epsilon_0}{k_B T_b}} \phi_2(T_b), \quad \text{(dimension m}^3\text{/s)}\qquad (44)$$

$$\phi_2(T_b) = 0.448 \ln(\epsilon_0/(k_B T_b)) \quad \text{(dimensionless)}.\qquad (45)$$

Finally the visibility function is defined by

$$\tilde{g}(x) = -\tau' e^{-\tau}, \quad \int_{-\infty}^0 \tilde{g}(x) dx = 1.\qquad (46)$$

So it is a probability distribution over $x$ and $\tilde{g}(x')$ denotes the probability (density) that a photon we observe today was last scattered at $x = x'$.

### 3.2. Implementation details

Although all the results in this paper will be taking into account helium, for completeness we do also implement and discuss the Saha equation, where the helium is absent. These two implementations produce the same results when setting $Y_p = 0$. In the Saha regime we will define one method for computing $X_e$ where we ignore helium. Then the Saha equation (29) has to be solved. This is a simple quadratic equation, of the form $ax^2 + bx + c = 0$, so could in principle be solved using the standard formula $x = \frac{-b \pm \sqrt{b^2 - 4ac}}{2a}$. But that solution will not be stable here because we will get

$$X_e = \frac{1}{2} C \left[ -1 + \sqrt{1 + 4/C} \right].$$

The "+" in front of the square root is because $X_e$ has to be positive. Early on, when $T_b$ is very high, C will also be large. So $X_e = \frac{1}{2} C \left( -1 + 1 \sqrt{1 + 4/C} \right) \approx \frac{1}{2} C \left( -1 + 1 + \frac{2}{C} \right) = 1$. Having

$-1 + 1 + \epsilon$, with $\epsilon$ being very small, is not numerically stable. So we will instead use the so-called "citardauq" equation, which is generally given by

$$x = \frac{2c}{-b \mp \sqrt{b^2 - 4ac}}.\qquad (47)$$

Here $a = 1, b = C, c = -C$, so

$$X_e = \frac{-2C}{-C - \sqrt{C^2 + 4C}} = \frac{2}{1 + \sqrt{1 + 4/C}}\qquad (48)$$

$$\approx \frac{2}{1 + (1 + 2/C)} = \frac{1}{1 + 1/C}.\qquad (49)$$

(The minus sign in front of the square root in the first line is again chosen to get a positive result). Equation (49) can be used to compute the electron fraction in the beginning, when $X_e \approx 1$ (and in the absence of helium). Then we transition to using the Peebles equation when $X_e$ starts to deviate from 1. Here that threshold has been chosen as $X_e = 0.99$, such that for $X_e > 0.99$ we use Saha's equation and for $X_e < 0.99$ we use Peebles' equation.

In the other method (the one we will be using) we include helium, in which case we have to solve (31), (32) and (33). This can be done iteratively by first guessing a $f_e \approx 1$, then calculating $n_e = f_e n_b$. Equations (31), (32) and (33) can then be rewritten into

$$x_{\text{He+}} = \frac{C_1}{n_e + C_1 + \frac{C_1 C_2}{n_e}},$$

$$x_{\text{He++}} = \frac{C_2}{n_e} x_{\text{He+}},$$

$$x_{\text{H+}} = \frac{C_3}{n_e + C_3},$$

where $C_1, C_2$ and $C_3$ are the right hand sides of (31), (32) and (33) respectively. See Appendix B.1 for a derivation of this. These $x_{\text{He+}}$, $x_{\text{He++}}$ and $x_{\text{H+}}$ can then be used to calculate a new value of $f_e$ from equation (34). We then use this new value of $f_e$ as our guess, and calculate $n_e$ again etc. This is done iteratively until the error $\left| f_e^{i+1} - f_e^i \right| < 10^{-10}$ for every value of $x$. Here superscript $i$ means the value at iteration $i$.

The differential equations (35) and (28) will be solved using the same ODE-solver as in Milestone I. In order to avoid numerical instability we insert (43) into (42) and get

$$\beta^{(2)}(T_b) = \alpha^{(2)} \left( \frac{m_e k_B T_b}{2\pi\hbar^2} \right)^{3/2} e^{-\epsilon_0/(4k_B T_b)},\qquad (50)$$

which avoids blowing up when $T_b$ is low.

### 3.3. Results

We compute $X_e$ and $n_e$ for 4000 linearly spaced $x$-values in the range $x \in \left[ \log_{10}\left(10^{-8}\right), 0 \right]$, and included helium by implement-

ing (31), (32) and (33) and setting $Y_p = 0.245$. When $X_e < 0.99$ we switch over to using Peebles' equation.

The time of recombination and the time of decoupling between photons and baryons are of interest. The former is when a significant amount of electrons start being bound in atoms, while the latter is when the interaction rate between photons and baryons becomes small and the universe becomes optically thin to photons. The time of recombination can be approximated as the time when $X_e = 0.5$, since half of the electrons are then bound in atoms. And the time of decoupling can be approximated as the time when $\tau(x)$ drops below 1, since the universe then becomes optically thin. We got

| Event | Redshift $z$ | $x$ | Time $t$ [Gyr] |
|---|---|---|---|
| Recombination | 1274 | -7.15 | $3.1 \cdot 10^{-4}$ |
| Decoupling | 1088 | -6.99 | $4.1 \cdot 10^{-4}$ |

**Table 2.** Points at which recombination and decoupling occur. They are given in terms of redshift, time and $x$. $t$ is given in Gyr.

The times of recombination and decoupling were also computed in the absence of helium, which gave the same results as in Table 2, where we have included helium. This reason for this is shown in Figure 11. After helium has recombined the two approaches overlap, so they will naturally agree on the times of recombination and decoupling.

The time of recombination can also be estimated using the Saha equation. Inserting $X_e = 0.5$ into (29) we get an equation for $T_b$. Since $T_b = T_\gamma = \frac{T_{CMB0}}{a} = T_{CMB0}e^{-x}$ this can be restated into an equation for $x$. This equation has to be solved numerically, and this gave $X_e = 0.5$ at $x \approx -7.23$. That is close to the more accurate solution from Peebles' equation, but a bit earlier. Figure 11 shows the electron fraction $X_e$ as a function of $x$ for $x \in [-10, -3]$. The dotted red line represents the solution in the absence of helium, while the solid blue curve represents the solution with helium taken into account. The dashed vertical line represents the time of decoupling, while the dotted vertical line represents the time of recombination (from Peebles' equation).
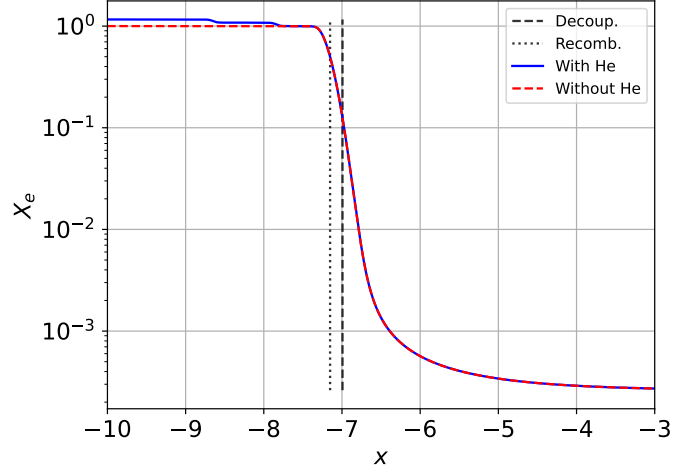


**Fig. 11.** Electron fraction as a function of $x$. The dotted red line represents the solution in the absence of helium, while the solid blue curve represents the solution with helium taken into account. The dashed and dotted vertical lines represent the $x$ at which decoupling and recombination occurred, respectively. The $x$-axis is limited to $x \in [-10, -3]$ to more easily see the changes in $X_e$ around recombination. The electron fraction (with helium) starts off at $\sim 1.2$ at early times. Then there are two drops in $X_e$ when electrons are bound in $He^+$ and $He$. Around $x \approx 7$ electrons are bound in hydrogen, causing a huge drop in $X_e$. Without helium the electron fraction is constant at $\sim 1$ until recombination, after which the two curves overlap. The $y$-axis is in logscale.

The electron fraction stays close to 1.2 for $x \lesssim -9$. This is in the very early universe when the temperature is very high. All the hydrogen and helium atoms are ionised (helium is doubly ionised). So $n_{He^{++}} = n_{He}$, $n_{He^+} = 0$ and $n_{H^+} = n_H$. Then

$$X_e = \frac{n_e}{n_H} = \frac{n_{H^+} + n_{He^+} + 2n_{He^{++}}}{n_H} = 1 + 2\frac{n_{He}}{n_H} = 1 + \frac{1}{2}\frac{Y_p}{1 - Y_p},$$

because $Y_p = \frac{4n_{He}}{n_b}$. Here we have used $Y_p = 0.245$, so $X_e \approx 1.16$. So the low-$x$ regime is in agreement with this. The first decrease in $X_e$ is when the doubly ionised helium ions take in an electron and become singly ionised. Then these ions take another electron some time later, at which point the electron fraction drops to 1. This is the regime when all electrons belonging to helium atoms are bound in helium, so the only free electrons around are those belonging to hydrogen. Meaning $n_e = n_H$, so $X_e = 1$ agrees with expectations. Around $x = -7$ the temperature is low enough for electrons to be bound in hydrogen, at which point the electron fraction drops almost to zero. However, not all the electrons are bound in atoms, the freeze-out abundance ($X_e$ today) is $X_e(x = 0) \approx 2.6 \cdot 10^{-4}$. This is because after a certain time the baryon density becomes so low that a free electron rarely encounters a proton, so these remaining free electrons are unable to be bound in atoms. The temperature at which recombination takes place is $T_b \approx T_\gamma \approx 0.3$ eV, which is much lower than the ionisation energy of hydrogen. $T_\gamma \approx \epsilon_0 = 13.6$ eV is when one would naively expect recombination to happen because the photons would not have enough energy to break apart a hydrogen atom after that point. But this balance is shifted by the tiny baryon-to-photon ratio. So even though there are few photons with high enough energy to ionise hydrogen around say 1 eV, there are many enough to ionise the relatively few baryons. The freeze-out abundance is $X_e$ (today) $\approx 2.6 \cdot 10^{-4}$. So there are very

few free electrons today (ignoring reionization, which we have not considered here).

Figure 12 shows the optical depth and its first two derivatives with respect to $x$ plotted as functions of $x$. The blue curve represents $\tau(x)$, the green curve $-\tau'(x)$ and the red curve $\tau''(x)$. The $x$-range is $x \in [-12, 0]$, and the $y$-axis is now logarithmic. The dashed and dotted vertical lines again denote decoupling and recombination.
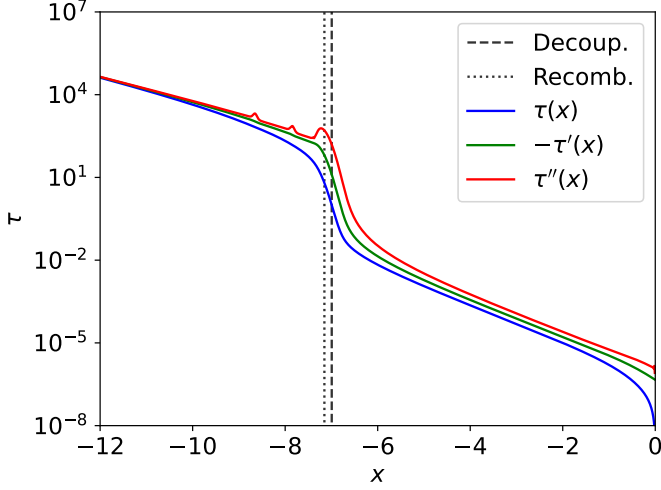


**Fig. 12.** The optical depth and its derivatives as functions of $x$. The dashed and dotted lines again represent decoupling and recombination. The blue curve represents $\tau(x)$, the green curve is $-\tau'(x)$ and the red curve is $\tau''(x)$. The $x$-axis is again limited to $x \in [-12, 0]$ and the $y$-axis is now logarithmic.

At early times ($x < -9$) the optical depth is at least of order $\sim 10^2$, meaning the medium is very thick and photons only travel a very short distance before being scattered. But around recombination the optical depth starts decreasing quickly. The reason for this is of course that this is when electrons start being bound in atoms, so the number of free electrons that a photon can interact with is much lower. And the cross section for photons interacting with atoms is, as mentioned earlier, inversely proportional to the square of the mass of the interacting particle. So interactions with atoms are, as before, negligible. Shortly after, at decoupling, the optical depth drops below 1. The first derivative of the optical depth is given by $\tau'(x) = -\frac{c n_e \sigma_T}{H}$. Around the time of recombination $n_e$ drops, meaning the absolute value of $\tau'(x)$ also drops. This is seen in Figure 12. The second derivative $\tau''(x)$ has two smaller bumps before recombination. These correspond to the recombination of He$^{++}$ to He$^+$ and He$^+$ to He. When these processes occur the electron number density drops, as seen in Figure 11. The double derivative of $\tau$ can be written as

$$\tau'' = -\frac{c\sigma_T}{H}\frac{dn_e}{dx} + \frac{c n_e \sigma_T}{H^2} \cdot \frac{dH}{dx} \qquad (51)$$

The second term is the decrease in $\tau''$ due to the expansion of the universe, which causes the general decrease in $\tau''$ both before and after recombination. To a good approximation the first term is zero except at recombination. But around recombination

$n_e$ drops, so at that time the first term is positive. So we get a positive contribution to $\tau''$. This is what causes the slight increase in $\tau''$ at recombination. The same also holds for the recombination of helium, but the bumps are smaller because the change in $n_e$ is smaller. After recombination the change in $n_e$ is negligible again, so $\tau''$ continues to decrease due to the expansion.

Figure 13 shows the visibility function and its first two derivatives with respect to $x$ plotted against $x$. The curves are clearly very peaked around $x = -7$, and approximately zero everywhere else. In order to see details in the curves we show a zoomed in view in Figure 14. Here the $x$-range has been limited to $x \in [-7.5, -6.2]$. The curves have been scaled to fit in the same plot. So the curves that are plotted are $\tilde{g}$, $\frac{\tilde{g}'}{10}$ and $\frac{\tilde{g}''}{200}$. The dashed and dotted vertical lines again show the time of decoupling and recombination.
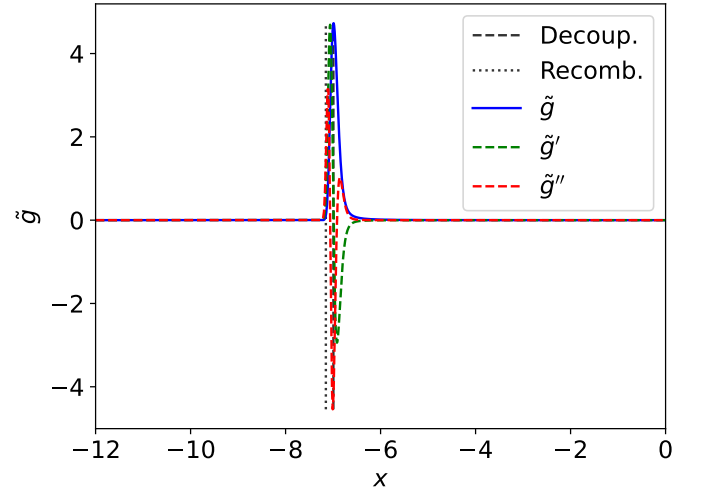


**Fig. 13.** The visibility function and its derivatives as functions of $x$. The dashed and dotted vertical lines still represent decoupling and recombination. The blue curve is $\tilde{g}(x)$, the green curve is $\tilde{g}'(x)$ and the red curve is $\tilde{g}''(x)$. The $x$-range is $\in [-12, 0]$. The curves have been scaled to fit in the same plot. So the curves that are plotted are $\tilde{g}$, $\frac{\tilde{g}'}{10}$ and $\frac{\tilde{g}''}{200}$
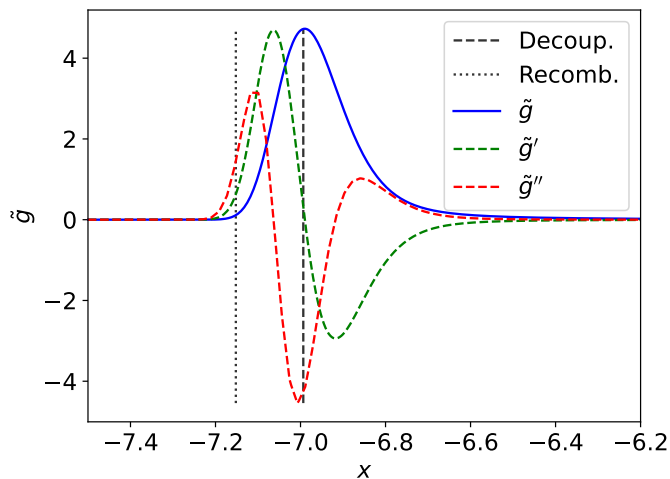
**Fig. 14.** The visibility function and its derivatives as functions of $x$. The dashed and dotted lines still represent decoupling and recombination. The blue curve is $\tilde{g}(x)$, the green curve is $\tilde{g}'(x)$ and the red curve is $\tilde{g}''(x)$. This time the $x$-axis has been limited to $x \in [-7.5, -6.2]$ because the peak in $\tilde{g}(x)$ (and hence also the other two) is so narrow. The curves have been scaled to fit in the same plot. So the curves that are plotted are $\tilde{g}$, $\frac{\tilde{g}'}{10}$ and $\frac{\tilde{g}''}{200}$

Figure 13 shows that the visibility function is highly peaked around the time of decoupling. This means that almost all the photons last scattered around the time of decoupling, which is what we would expect. This of course implies that practically all the photons that we observe in the CMB today come from the gas at around $-7.2 \leq x \leq -6.6$. So we are seeing the gas from around this time, corresponding to a redshift of $z \approx 1100$. The visibility function is not symmetric around the time of decoupling. That is because after decoupling there were a few photons that were able to interact with electrons even after decoupling. So they were last scattered shortly after decoupling. But almost all of the photons that scattered some time before decoupling also scattered at a later time around decoupling, since $\tau > 1$ before decoupling. So very few photons scattered for the last time before decoupling, which is why the left tail of $\tilde{g}$ is more suppressed than the right tail.

The derivatives of the visibility function are also as expected. The rate of change of the visibility function has a maximum at a time between recombination and decoupling, because the electron fraction decreases most rapidly in that period. So right before recombination the probability of a photon scattering for the last time increases. And after recombination the probability decreases. The double derivative has a maximum some time shortly after recombination, meaning the increase in the visibility function is accelerating right after recombination. The minimum in $g''(x)$ around recombination just means the visibility function goes from increasing to decreasing at recombination. That is in accordance with the discussion here.

## 4. Milestone III

Up until now we have assumed a smooth universe in which none of the physical quantities have a spatial dependence. That is of course not sufficient if we want to predict the CMB power spectrum - we need to introduce perturbations in all the quantities. All these spatial perturbations will then evolve over time,

so we will also need to solve for the time evolution of the different perturbations. This can in principle get very complicated, but fortunately the perturbations are small. So we can safely work in linear perturbation theory, neglecting all 2nd or higher order terms in the perturbations. We will be working in Fourier space rather than in real space, and the PDEs in real space will then be transformed to ODEs in Fourier space. And since we work in linear perturbation theory the evolution of each Fourier mode is independent of all the other modes. This is a huge simplification, and we can solve for the evolution of each mode separately. These different modes correspond to different physical scales, so when we have solved for the evolution of the perturbations for a certain mode then we know how that scale evolves over time. This will be very useful when computing the power spectrum later.

### 4.1. Theory

For each of the components $i$ in the universe we can formulate the Boltzmann equation

$$\frac{df_i}{d\lambda} = C(f_i, f_j, f_k, ...) \tag{52}$$

where $f_i$ is the distribution function for a species $i$, describing the number of particles of species $i$ in each phase space volume. $\lambda$ is an affine parameter along the particle's path. $C(f_i, f_j, f_k)$ is the collision term describing the interaction between particles, and it can in principle depend on all the species in the universe. Here $i$ will represent photons, baryons and dark matter, so we will use the Boltzmann equation in order to solve for the evolution of the photon-, baryon- and dark matter-perturbations (neglecting neutrinos). Deriving the evolution equations for the perturbation variables proceeds in three main steps:

1. Rewrite the Boltzmann equation by expanding the $\frac{d}{d\lambda}$ as a total derivative, taking into account the dependence of $f_i$ on time, position and momentum.
2. Use expressions for $\frac{dt}{d\lambda}$ and $\frac{dx^i}{d\lambda}$ from the geodesic equations in a universe with a perturbed FRW metric.
3. The way to proceed now depends on the species in question. But the general procedure involves expanding a quantity in the smooth background part plus a perturbed part. This can then be used to formulate evolution equations for the perturbation variables.

A detailed analysis and derivation of the evolution equation for each perturbation variable can be found in Winther (2021) or Dodelson (2011). The equations are then also transformed into Fourier space, which is where we will be working in the rest of the paper. In these derivations we always neglect terms higher order in the perturbations, since we work in linear perturbation theory. The perturbation variables for the baryons are the density perturbation and the bulk velocity, $\delta_b$ and $v_b$ respectively. $\delta_b$ describes the deviation from the mean baryon density and $v_b$ decsribes the bulk velocity of a collection of baryons in a certain position. For cold dark matter it is exactly the same, $\delta_{\text{CDM}}$ and $v_{\text{CDM}}$. The temperature perturbation of photons, $\Theta$, describing the deviation from the mean photon temperature, can be expanded in multipoles, $\Theta_0, \Theta_1, \Theta_2, ...$ These multipoles describe the angular dependence of the temperature perturbation at a given position. $\Theta_0$ is the monopole, describing the mean

temperature at a given position. $\Theta_1$ is the dipole, describing the velocity of the photon fluid (which is given by $v_\gamma = -3\Theta_1$). It is just the Doppler effect, caused by the motion of the photons. The higher order multipoles get increasingly more difficult to provide an intuitive explanation for, but the photon temperature perturbation $\Theta$ can nevertheless be expanded as

$$\Theta(t, k, \mu) = \sum \frac{2\ell + 1}{i^\ell} \Theta_\ell(t, k) P_\ell(\mu) \tag{53}$$

where $k$ is the Fourier wave number and $\mu = \frac{\hat{p} \cdot \mathbf{k}}{k}$, where $\hat{p}$ is the unit vector along the photon propagation direction and $\mathbf{k}$ is the Fourier wave vector. $P_\ell(\mu)$ are the Legendre polynomials, which are again explained more in detail in Winther (2021). The multipoles can be computed using

$$\Theta_\ell = \frac{i^\ell}{2} \int_{-1}^{1} \Theta(t, k, \mu) P_\ell(\mu) d\mu \tag{54}$$

Before proceeding we just make explicit how we relate these perturbations to the total physical quantities $\rho_{\text{CDM}}$, $T_\gamma$ etc.

$$\rho_{\text{CDM}}(t, \mathbf{x}) = \bar{\rho}_{\text{CDM}}(t)\left(1 + \delta_{\text{CDM}}(t, \mathbf{x})\right) \tag{55}$$

$$\rho_b(t, \mathbf{x}) = \bar{\rho}_b\left(1 + \delta_b(t, \mathbf{x})\right) \tag{56}$$

$$T_\gamma = \bar{T}_\gamma(1 + \Theta(t, \mathbf{x}, p, \hat{p})) \tag{57}$$

where $T_\gamma$ is the photon temperature. All quantities with a bar denote the background quantities in the smooth universe. We have not included $v_{\text{CDM}}$ and $v_b$ in this list because in the smooth universe these are zero, as there is no bulk velocity. So the velocity of the dark matter or baryons is purely the perturbed velocity. The perturbed FRW metric takes the form

$$ds^2 = -dt^2(1 + 2\Psi) + a^2(1 + 2\Phi)(dx^2 + dy^2 + dz^2) \tag{58}$$

with $\Psi$ and $\Phi$ being perturbation variables, and they are closely related to the Newtonian potential. See Winther (2021) for more details.

We are then ready to write down all the evolution equations for the perturbations that have been introduced. First for the photon multipoles

$$\Theta_0' = -\frac{ck}{\mathcal{H}}\Theta_1 - \Phi', \tag{59}$$

$$\Theta_1' = \frac{ck}{3\mathcal{H}}\Theta_0 - \frac{2ck}{3\mathcal{H}}\Theta_2 + \frac{ck}{3\mathcal{H}}\Psi + \tau'\left[\Theta_1 + \frac{1}{3}v_b\right], \tag{60}$$

$$\Theta_\ell' = \frac{\ell ck}{(2\ell + 1)\mathcal{H}}\Theta_{\ell-1} - \frac{(\ell + 1)ck}{(2\ell + 1)\mathcal{H}}\Theta_{\ell+1}$$
$$+ \tau'\left[\Theta_\ell - \frac{1}{10}\Pi\delta_{\ell,2}\right], \qquad 2 \le \ell < \ell_{\max} \tag{61}$$

$$\Theta_\ell' = \frac{ck}{\mathcal{H}}\Theta_{\ell-1} - c\frac{\ell + 1}{\mathcal{H}\eta(x)}\Theta_\ell + \tau'\Theta_\ell, \qquad \ell = \ell_{\max}, . \tag{62}$$

Then for the cold dark matter and baryons

$$\delta_{\text{CDM}}' = \frac{ck}{\mathcal{H}}v_{\text{CDM}} - 3\Phi' \tag{63}$$

$$v_{\text{CDM}}' = -v_{\text{CDM}} - \frac{ck}{\mathcal{H}}\Psi \tag{64}$$

$$\delta_b' = \frac{ck}{\mathcal{H}}v_b - 3\Phi' \tag{65}$$

$$v_b' = -v_b - \frac{ck}{\mathcal{H}}\Psi + \tau'R(3\Theta_1 + v_b). \tag{66}$$

And finally for the metric perturbations

$$\Phi' = \Psi - \frac{c^2k^2}{3\mathcal{H}^2}\Phi + \frac{H_0^2}{2\mathcal{H}^2}\left[\Omega_{\text{CDM}0}a^{-1}\delta_{\text{CDM}} + \Omega_{b0}a^{-1}\delta_b + 4\Omega_{\gamma 0}a^{-2}\Theta_0\right] \tag{67}$$

$$\Psi = -\Phi - \frac{12H_0^2}{c^2k^2a^2}\Omega_{\gamma 0}\Theta_2. \tag{68}$$

In all of these $f' = \frac{df}{dx}$ for some quantity $f$. $\Pi = \Theta_2 + \Theta_0^P + \Theta_2^P$ in general, where $\Theta_l^P$ are polarization multipoles of the photons. But here we will neglect polarization, so $\Pi$ can just be replaced by $\Theta_2$. In general there would also be extra terms in $\Phi'$ and $\Psi$ accounting for the contribution of neutrinos to the metric perturbations, but as mentioned previously, we will neglect neutrinos as well. And $R = \frac{4\Omega_{\gamma 0}}{3\Omega_{b0}a}$. The terms involving $\tau'$ in the photon multipoles and baryon velocity represent momentum transfer between the photons and baryons. This momentum transfer is caused by the Compton scattering between photons and free electrons.

When we compute the CMB power spectrum later it turns out we will only need to have solved for the evolution of the first three multipoles for the photon temperature. This is due to a method called line of sight integration, which will be introduced in the next milestone. So in principle one might think that we do not actually need to solve for $\Theta_3, \Theta_4$ etc. here. But in practice we do, because we need accurate values for the first three multipoles. And if we were to truncate the multipole series at $\Theta_2$ then the multipoles that we actually need would quickly become inaccurate. But the line of sight integration scheme means that we only need to solve $\Theta_l'$ for a sufficient number of multipoles such that the values for $\Theta_0, \Theta_1$ and $\Theta_2$ are accurate. The $l_{\max}$ in equations (61) and (62) is thus the $l$ corresponding to the highest order multipole that we include. As is clear from the aforementioned equations, the form of $\Theta_l'$ for the last multipole is slightly different from the lower order multipoles. This is because instead of just truncation the multipole series at $l_{\max} - 1$ and setting $\Theta_{l_{\max}} = 0$ we use a modified expression for $\Theta_{l_{\max}}$. The expression in equation (62) is derived in Callin (2006) and is based on looking at the behaviour of $\Theta_l$ for large $l$.

Equations (59) - (68) form a closed, coupled set of ODEs. But in order to solve the system we need initial conditions. These are set up by inflation, which is discussed in more detail in Winther (2021) and Dodelson (2011). Briefly, we can define the so-called curvature perturbation as

$$\mathcal{R} = \Phi + \frac{\mathcal{H}^2(\frac{d\Phi}{d\log a} - \Psi)}{4\pi G a^2(\bar{\rho} + \bar{P})}, \tag{69}$$

where $\bar{\rho}$ and $\bar{P}$ are the background density and pressure. This quantity has the property that $\frac{d\mathcal{R}}{dt} \approx 0$ for a mode outside the horizon (meaning $ck \ll \mathcal{H}$). For any such mode then, the value of $\mathcal{R}$ set up during inflation will be the same after it exits the horizon, and until it enters the horizon after inflation has ended. And all the modes that will be of interest to us were outside the horizon in the very early universe. So if we know the value of $\mathcal{R}$ for a certain mode during inflation then we also know its value when the mode enters the horizon. The goal is then to be able to relate the physical quantities of interest here to $\mathcal{R}$, such that we can draw our initial conditions from the value of $\mathcal{R}$ during inflation. There are different ways of doing this, and the initial conditions we will use are called adiabatic initial conditions. These are based on assuming that the conditions at a point $\boldsymbol{x}$ at time $t$ are given by the conditions of the background universe at some different time $t + \Delta t(\boldsymbol{x})$. The details are given in Winther (2021) and in Baumann (2015). The result of their analyses is that the initial conditions are

$$\Psi = -\frac{2}{3} \tag{70}$$

$$\Phi = -\Psi \tag{71}$$

$$\delta_{\text{CDM}} = \delta_b = -\frac{3}{2}\Psi \tag{72}$$

$$v_{\text{CDM}} = v_b = -\frac{ck}{2\mathcal{H}}\Psi \tag{73}$$

Photons:

$$\Theta_0 = -\frac{1}{2}\Psi \tag{74}$$

$$\Theta_1 = +\frac{ck}{6\mathcal{H}}\Psi \tag{75}$$

$$\Theta_2 = -\frac{20ck}{45\mathcal{H}\tau'}\Theta_1 \tag{76}$$

$$\Theta_\ell = -\frac{\ell}{2\ell + 1}\frac{ck}{\mathcal{H}\tau'}\Theta_{\ell-1}, \qquad \ell > 2 \tag{77}$$

The normalization of these initial conditions is such that $\mathcal{R} = 1$. We can normalize any way we want because the system of ODEs is linear. This will of course mean that the values we get when solving for the perturbation variables can be much larger than 1. So it seems like linear perturbation theory may not be accurate after all. But it is important to note that we can rescale our variables here however we like, the physics does not care. The actual values of the perturbation variables are orders of magnitude smaller than 1. So this rescaling is just a simple trick when computing the quantities we want, it does not mean linear perturbation theory is inaccurate.

In principle we can now solve this system for the interval of time we are interested in. But in the early universe $\tau'$ is very large. And $\Theta_1 + \frac{1}{3}v_b = \frac{1}{3}\left(v_\gamma - v_b\right)$ is very close to zero due to the tight coupling between the photons and baryons. So the product $\tau'\left[\Theta_1 + \frac{1}{3}v_b\right]$ is very numerically unstable. The regime during which this is problematic is the so-called tight coupling regime. In this regime we will use the following expressions for $\Theta_1$ and $v_b$, derived in Winther (2022c).

$$q = \frac{-[(1 - R)\tau' + (1 + R)\tau''](3\Theta_1 + v_b) - \frac{ck}{\mathcal{H}}\Psi}{(1 + R)\tau' + \frac{\mathcal{H}'}{\mathcal{H}} - 1}$$
$$+ \frac{(1 - \frac{\mathcal{H}'}{\mathcal{H}})\frac{ck}{\mathcal{H}}(-\Theta_0 + 2\Theta_2) - \frac{ck}{\mathcal{H}}\Theta_0'}{(1 + R)\tau' + \frac{\mathcal{H}'}{\mathcal{H}} - 1} \tag{78}$$

$$v_b' = \frac{1}{1 + R}\left[-v_b - \frac{ck}{\mathcal{H}}\Psi + R(q + \frac{ck}{\mathcal{H}}(-\Theta_0 + 2\Theta_2) - \frac{ck}{\mathcal{H}}\Psi)\right] \tag{79}$$

$$\Theta_1' = \frac{1}{3}(q - v_b') \tag{80}$$

This is done in order to avoid the numerical instability. The higher order multipoles in this regime are given by

$$\Theta_2 = -\frac{20ck}{45\mathcal{H}\tau'}\Theta_1, \tag{81}$$

$$\Theta_\ell = -\frac{\ell}{2\ell + 1}\frac{ck}{\mathcal{H}\tau'}\Theta_{\ell-1}, \qquad \ell > 2, \tag{82}$$

which are the same expressions as for the initial conditions. In the discussion in the results-section, when saying that a mode "enters the horizon" we mean that the scale corresponding to the mode in question is small enough that it is comparable to the size of the horizon. More compactly a mode enters the horizon when $k\eta \sim 1 \iff \frac{ck}{\mathcal{H}} \sim 1$ (since $\eta \sim \frac{c}{\mathcal{H}}$). $\frac{ck}{\mathcal{H}} \ll 1$ for a mode outside the horizon and $\frac{ck}{\mathcal{H}} \gg 1$ for a mode inside the horizon.

### 4.2. Implementation details

Because of the transformation into Fourier space we can solve the differential equations separately for each $k$. And as discussed in the previous section we need to solve for the evolution of the perturbations in two steps; the tight coupling regime, and after tight coupling ends. During tight coupling we use equations (78), (79) and (80) to find $v_b'$ and $\Theta_1'$. $\Theta_0', \delta_b', \delta_{\text{CDM}}', v_{\text{cdm}}', \Psi$ and $\Phi'$ are given by the same expressions as after tight coupling. The higher order photon multipoles, however, are given by equations (81) and (82). These have $\tau'$ in the denominator, and since $\tau'$ is very large during tight coupling they will be heavily suppressed during this regime. We will thus not have differential equations describing these higher order multipoles during tight coupling, rather we will have the algebraic expressions. So in this regime the set of ODEs consists of $\{\Theta_0', \Theta_1', \delta_{\text{CDM}}', v_{\text{CDM}}', \delta_b', v_b', \Phi'\}$. The same ODE-solver as in milestone I and II can thus be used, just that we are now sending in a vector of 7 different quantities. The right hand side of the ODE-system will then correspondingly have to be a vector containing the right hand sides of $\Theta_0', \Theta_1'$ etc. We can then choose some initial time $x_{\text{start}}$ to integrate from. The initial conditions are those given in equation (70) - (75).

We will have to choose some criterion for when tight coupling should end. Tight coupling is when $\tau'$ is large, so the criterion should be on $\tau'$. We will follow the criteria used in Callin (2006). The scheme is that tight coupling ends when one of the following criteria is met.

1. $\tau' < 10$

2. $\left|\frac{ck}{\mathcal{H}\tau'}\right| < \frac{1}{10}$

3. We approach recombination, so $X_e < 1$

The first criterion is because tight coupling should end when $\tau'$ starts becoming small. The second one is to make sure tight coupling ends at the latest around the time when the mode enters the horizon, $\frac{ck}{\mathcal{H}} \sim 1$. And the last criterion is to make sure tight coupling ends when recombination starts kicking in.

After having solved this system in the tight coupling regime we can then calculate the values of all the higher order multipoles at each point in time during that regime. Then we use the values for all the perturbations, including the higher order multipoles, at the last time step in tight coupling as initial conditions for the full system (equations (59)-(68)). Our system of ODEs is now $\left\{\Theta'_0, \Theta'_1, \Theta'_2, ..., \Theta'_{l_{max}}, \delta'_{CDM}, v'_{CDM}, \delta'_b, v'_b, \Phi'\right\}$, and solving this is exactly the same as solving the previous system of ODEs. The solutions in and after tight coupling can then be combined, so that we have arrays containing the values of all the perturbations from $x_{start}$ to our endpoint $x_{end}$. These arrays can finally be splined to allow for interpolation.

We use linearly spaced $x$-values and logarithmically spaced $k$-values, because the $k$-values will range over multiple orders of magnitude. The numbers of points to use for $x$ and $k$ are then chosen to get accurate results while having a reasonable runtime. This is mostly just done through trial and error.

A useful side note is that since all the different $k$'s evolve independently this system lends itself very naturally to parallelization in the code. This allows for much quicker code, since the ODEs for different $k$'s can be solved simultaneously.

### 4.3. Results

When solving the differential equations we used 1000 linearly spaced $x$-values in the range $\left[\log\left(10^{-8}\right), 0\right]$ and 100 logarithmically spaced $k$-values in the range $k \in \left[5 \cdot 10^{-5}, 0.3\right]$ Mpc$^{-1}$. We include 8 photon multipoles, so $l_{max} = 7$. And when plotting the results we use 5000 linearly spaced $x$-values in the range $x \in \left[\log\left(10^{-8}\right), 0\right]$. We compute and plot the perturbation variables for $k = \{0.3, 0.05, 0.0001\}$ Mpc$^{-1}$. The following figures show the evolution of the different perturbation variables as a function of $x$ for the three values of $k$. Figures 15, 16, 17, 18, 19 and 20 represent $(\delta_{CDM}, \delta_b)$, $\Theta_0$, $(v_{CDM}, v_b)$, $\Theta_1$, $\Phi$ and $\Psi$ respectively (the parentheses just means we have plotted CDM and baryons together). In all the figures the blue curve corresponds to $k = 0.3$/Mpc, red to $k = 0.05$/Mpc and green to $k = 0.0001$/Mpc. And in Figure 15 and 17 the dashed curves correspond to baryons while the solid curves correspond to dark matter. In these two figures we have plotted the absolute value of the baryon density perturbation and velocity perturbation respectively, since these are also negative at times. The dashed vertical line in all the figures represents the time of decoupling and the dotted vertical line represents the time of matter-radiation equality. All the figures have $x$-range $[\log\left(10^{-8}\right), 0]$. Also keep in mind the normalization we have used here. The actual values are not important, since the normalization is arbitrarily chosen. only the evolution of the perturbations is important.

The reason for explicitly showing the times of matter-radiation equality and decoupling of photons and baryons is that these times are important for how the perturbations evolve. Whether a mode enters the horizon before or after matter-radiation equality will play an important role in the evolution of the perturbation, while decoupling is important to the way the evolution of the baryon perturbations changes at this point. These aspects are discussed in detail below.
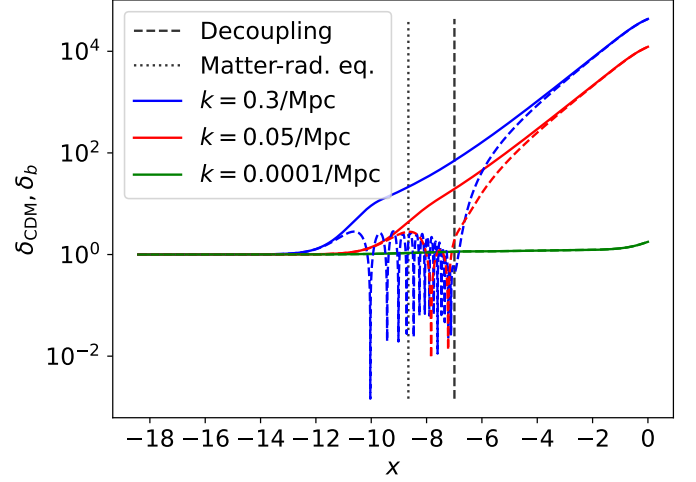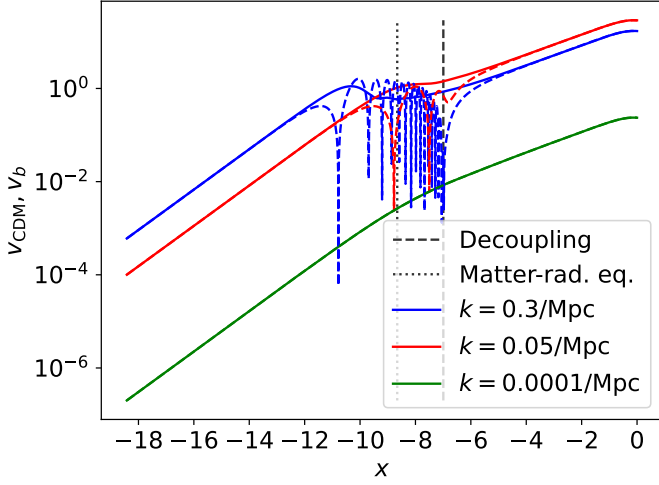


**Fig. 15.** Density perturbations in the cold dark matter and baryons as functions of $x$. The dashed curves are for the baryons, where we have plotted the absolute value of $\delta_b$. And the solid curves are for the dark matter. Blue represents $k = 0.3$/Mpc, red is for $k = 0.05$/Mpc and green for $k = 0.0001$/Mpc. The dashed vertical line represents the time of decoupling, while the dotted vertical line represents the time of matter-radiation equality. The $x$-range is $[\log\left(10^{-8}\right), 0]$, and the $y$-axis is logarithmic.
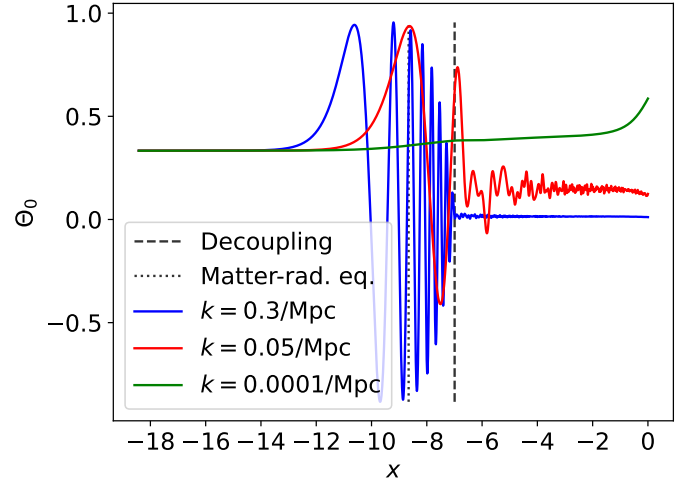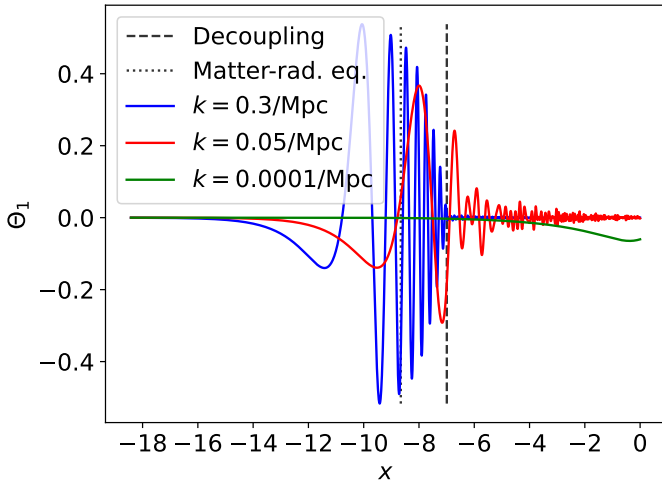


**Fig. 16.** The photon temperature monopole for different $k$ as functions of $x$. The monopole corresponds to a density perturbation. Blue represents $k = 0.3$/Mpc, red is for $k = 0.05$/Mpc and green for $k = 0.0001$/Mpc. The dashed vertical line represents the time of decoupling, while the dotted vertical line represents the time of matter-radiation equality. The $x$-range is $[\log\left(10^{-8}\right), 0]$.
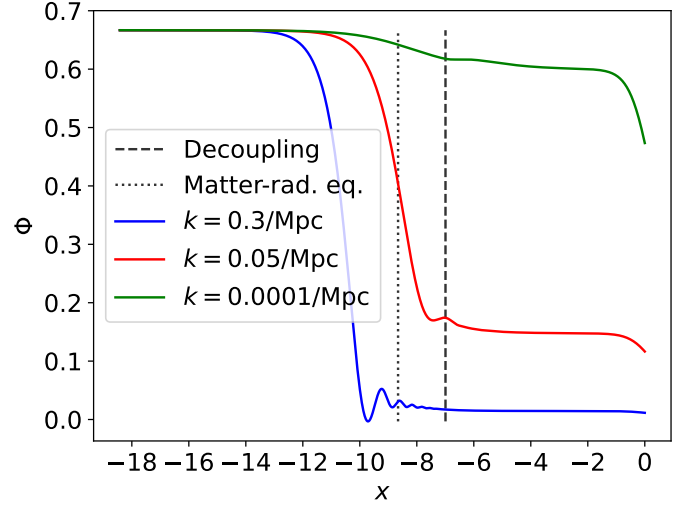
**Fig. 17.** Bulk velocities of the cold dark matter and baryons as functions of $x$. The dashed curves are for the baryons, again plotting the absolute value of $v_b$. And the solid curves are for the dark matter. Blue represents $k = 0.3/\text{Mpc}$, red is for $k = 0.05/\text{Mpc}$ and green for $k = 0.0001/\text{Mpc}$. The dashed vertical line represents the time of decoupling, while the dotted vertical line represents the time of matter-radiation equality. The $x$-range is $[\log(10^{-8}), 0]$ and the $y$-axis is logarithmic.



**Fig. 19.** The metric perturbation $\Phi$. Blue represents $k = 0.3/\text{Mpc}$, red is for $k = 0.05/\text{Mpc}$ and green for $k = 0.0001/\text{Mpc}$. The dashed vertical line represents the time of decoupling, while the dotted vertical line represents the time of matter-radiation equality. The $x$-range is $[\log(10^{-8}), 0]$.



**Fig. 18.** The photon temperature dipole for different $k$ as functions of $x$. The dipole corresponds to a bulk velocity of the photons. Blue represents $k = 0.3/\text{Mpc}$, red is for $k = 0.05/\text{Mpc}$ and green for $k = 0.0001/\text{Mpc}$. The dashed vertical line represents the time of decoupling, while the dotted vertical line represents the time of matter-radiation equality. The $x$-range is $[\log(10^{-8}), 0]$.
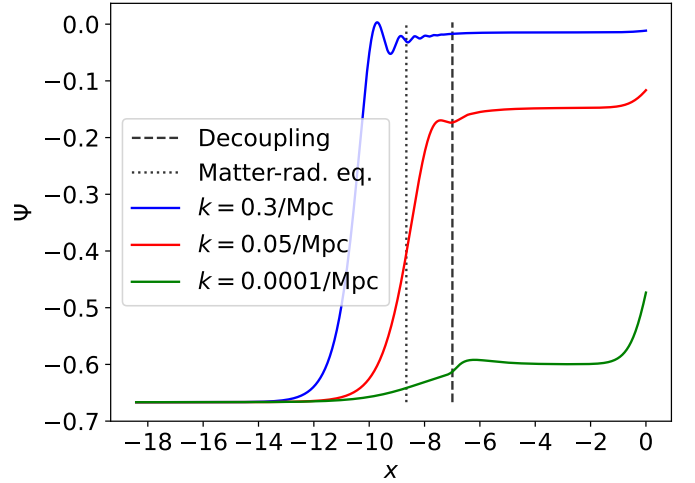


**Fig. 20.** The metric perturbation $\Psi$. Blue represents $k = 0.3/\text{Mpc}$, red is for $k = 0.05/\text{Mpc}$ and green for $k = 0.0001/\text{Mpc}$. The dashed vertical line represents the time of decoupling, while the dotted vertical line represents the time of matter-radiation equality. The $x$-range is $[\log(10^{-8}), 0]$.

At very early times all three scales are outside the horizon, meaning $\frac{ck}{\mathcal{H}} \ll 1$. This can of course be inferred explicitly from the value of $\mathcal{H}$ at early times, but an easy way to see it is from Figure 19 or 20. During very early times the potentials $\Phi$ and $\Psi$ stay constant, even though this is the radiation dominated era. From section 7.3 in Dodelson (2011) we know that for a mode $k$ entering the horizon during radiation domination the potential $\Phi$ evolves as

$$\Phi \propto \frac{\sin\left(k\eta/\sqrt{3}\right) - \left(k\eta/\sqrt{3}\right)\cos\left(k\eta/\sqrt{3}\right)}{\left(k\eta/\sqrt{3}\right)^3} \tag{83}$$

where $\eta$ is, as before, the conformal time. This is a decaying solution, so since the potentials are staying constant in the early universe they have to be outside the horizon.

It is then clear that the mode $k = 0.3$/Mpc enters the horizon at $x \approx -13$, since its potential starts decaying around that time. And we are still deep in the radiation dominated era. The reason for this decay when entering the horizon during radiation domination is straight forward. During this era the gravitational potential is set up by radiation alone[1], since this is the dominant form of energy at that time. And as soon as a mode enters the horizon the density perturbation, $\Theta_0$, will start oscillating. This is quite reasonable. The photon density perturbation initially increases as the mode enters the horizon. But then the pressure pushes the radiation away, decreasing the density. So we get an oscillation in the photon density perturbation $\Theta_0$. This is evident from the curve for $k = 0.3$/Mpc in Figure 16. So the density perturbation does not grow over time, it stays the same order of magnitude, but the universe expands. From equation (7.16) in Dodelson (2011) the potential during radiation domination is approximately given by

$$k^2\Phi = 16\pi G a^2 \rho_\gamma \Theta_0, \tag{84}$$

where we have neglected the contribution to the potential from matter, and neglected a term proportional to $\frac{\mathcal{H}}{k}$ because the mode is inside the horizon, so $\frac{\mathcal{H}}{k} \ll 1$. We know that $\rho_\gamma \propto a^{-4}$, so since $\Theta_0 \sim 1 \implies \Phi \propto a^{-2}$, hence the decay. Figure 16 shows that $\Theta_0$ is driven up to its maximum value early on (for $k = 0.3$/Mpc), and this is due to the decay of the potential. In Winther (2021) and Dodelson (2011) they derive that a decaying potential leads to a driving force for $\Theta_0$. This is called the radiation driving effect. So when the potential decays for $k = 0.3$/Mpc in the radiation dominated era this acts as a forcing term for $\Theta_0$, and the amplitude of the oscillations of $\Theta_0$ are thus driven up. After the potential more or less stabilizes around $x = -10$ there is no radiation driving effect anymore. And clearly $\Theta_0$ then starts decaying. This is due to the diffusion damping effect. Since the universe is not perfectly opaque even in the early universe the photons can travel a bit before they scatter. And so temperature perturbations on very small scales will be washed out, and thus damped. The scale at which this damping kicks in depends on the optical depth (or number density of free electrons, $n_e$) and expansion rate. From section 8.1 in Dodelson (2011) the damping scale is approximately

$$\lambda_{\mathrm{D}} = \frac{1}{\sqrt{n_e \sigma_T H}}, \tag{85}$$

meaning modes with $k > k_{\mathrm{D}} \sim \frac{1}{\lambda_{\mathrm{D}}} = \sqrt{n_e \sigma_T H}$ will be damped. The damping of a mode with $k > k_{\mathrm{D}}$ is by a factor $e^{-k^2/k_{\mathrm{D}}^2}$ (see Winther (2021) for instance). In the early universe, during matter-radiation domination $H \propto a^{-2}$ and $n_e \sim n_b \propto a^{-3}$, so $k_{\mathrm{D}} \sim \sqrt{a^{-3}a^{-2}} = a^{-5/2}$. So $k_{\mathrm{D}}$ decreases with time, and thus modes corresponding to larger and larger scales will be damped. So this is what happens with $k = 0.3$/Mpc in Figure 16. The mode is damped after radiation driving stops, so the amplitude of

---

[1] There is of course also matter, but its contribution is much smaller than that of radiation during this period.

the $\Theta_0$ oscillation decreases with time. And clearly the damping is huge right after decoupling. This is because the number density of free electrons, $n_e$, then drops roughly to zero, as we have seen earlier. And so the damping factor $e^{-k^2/k_{\mathrm{D}}^2}$ will be very small, and thus the amplitude of $\Theta_0$ is almost driven to zero. Physically this means that since the optical depth drops almost to zero the photons can travel very far before encountering anything. So even very large scale (small $k$) temperature perturbations will be washed out. The same effect can be seen for $k = 0.05$/Mpc, albeit not as strongly. This mode also enters the horizon during radiation domination, so the potential starts decaying (see Figure 19). This then drives up the amplitude of $\Theta_0$, but once this driving effect is gone the amplitude starts being damped, and after decoupling the damping is much stronger. The $k = 0.0001$/Mpc mode does not show this effect, it only has a radiation driving effect during its entry into the horizon during dark energy domination.

$k = 0.3$/Mpc is the largest of the three $k$'s, so corresponds to the smallest scale. It is therefore sensible that this scale should enter the horizon while the other (larger scale) modes are still outside. The potential for $k = 0.3$/Mpc decays during radiation domination and oscillates for a while, in accordance with equation (83). From Dodelson (2011) we know that for very large scale modes outside the horizon during the transition from radiation to matter domination the potential will drop by 10% during the transition. This is indeed the case for $k = 0.0001$/Mpc, and is again reasonable, since this is a very large scale mode. $k = 0.05$/Mpc is an intermediate-scale mode. It clearly drops by more than 10%, but not as much as for $k = 0.3$/Mpc. Close to today the potentials decay again, and this is due to dark energy. When dark energy starts dominating the expansion is so fast that the matter density perturbations can not grow, so the potentials decay.

Figure 15 shows how the matter density perturbations evolve. All the perturbations are outside the horizon until $x \approx -13$, at which point the $k = 0.3$/Mpc mode enters the horizon. And clearly the density perturbations do not grow while the modes are outside the horizon. As soon as the $k = 0.3$/Mpc mode enters the horizon $\delta_{\mathrm{CDM}}$ starts growing. The baryon density perturbation $\delta_b$ also initially starts growing, moving with the photons. But when the photons start oscillating in density the baryons follow because of the tight coupling between the two species. So the baryon density is not allowed to grow before decoupling. But after decoupling the baryons are not coupled to the photons anymore and can feel the potential set up by the dark matter. They start falling into these potential wells and the baryon density perturbation is allowed to grow with the dark matter. The same baryon-oscillation happens for the $k = 0.05$/Mpc mode, but to a lesser extent. This mode enters the horizon a shorter time before matter-radiation equality, so $\Theta_0$ is not able to oscillate nearly as long as for $k = 0.3$/Mpc. Then neither are the baryons, so the dark matter density perturbation is not able to get as much of a head start. The $k = 0.0001$/Mpc enters the horizon during dark energy domination, so a long time after decoupling. The fact that $\Theta_0$ is driven up by the decay of the potential is thus irrelevant for the baryon overdensity, since the baryons are decoupled from the photons at this point.

During matter domination the dark matter density for the $k = 0.3$/Mpc and $k = 0.05$/Mpc modes seems to grow like a power law in $a$ ($\log \delta_{\mathrm{CDM}} \propto n \log a = nx$, for some $n$). And this

is in accordance with Dodelson (2011), where they present the result $\delta_{CDM} \propto a$. This seems correct relative to Figure 15. It can also be justified by considering the potential during matter domination. From Dodelson (2011): $\Phi \propto a^2 \rho_{CDM} \delta_{CDM}$. We know that $\rho_{CDM} \propto a^{-3}$, so if $\Phi \approx$ const., as we see in Figure 19, then $\delta_{CDM} \propto a$.

Before the $k = 0.3$/Mpc mode enters the horizon the velocity of the perturbations in the baryons and dark matter is small. From equation (64) we see that $v'_{CDM} > 0$ if $-\frac{ck}{\mathcal{H}}\Psi > v_{CDM}$. The same holds for $v_b$ in the very early universe, since the baryons are so tightly coupled to the photons. And the photon perturbation velocity is $v_\gamma = -3\Theta_1$, so the last term in equation (66) is then zero, since the baryons and photons move together. The initial condition for $v_{CDM}$ and $v_b$ are $v_{CDM} = v_b = -\frac{ck}{2\mathcal{H}}\Psi$, so $v'_{CDM}$ is of order $\frac{ck}{\mathcal{H}}$ early on. Hence why $v_{CDM}$ and $v_b$ are very small in the early universe, when $\frac{ck}{\mathcal{H}} \ll 1$. The $k = 0.3$/Mpc mode enters the horizon before matter-radiation equality, and around $x = -10$ the velocity is large enough that $v_{CDM} < 0$. After a while, starting around matter-radiation equality, the mode is so far inside the horizon that $\frac{ck}{\mathcal{H}} \gg 1$, meaning the second term in equation (64) will dominate. And thus the velocity increases, since $\Psi < 0$.

Baryons will of course behave in a different way than dark matter after horizon entry for modes entering before decoupling. As discussed above they move with the photons before decoupling, so they also undergo oscillations. We have discussed how this is clear from Figure 15, but it is also apparent from Figure 17, both for $k = 0.3$/Mpc and $k = 0.05$/Mpc. After decoupling the baryons stop interacting with the photons, so the oscillatory motion of the baryons ceases. They can then fall into the potential wells of the dark matter and move together with the dark matter. For larger scale modes (smaller $k$) the effect is less dramatic, both for the dark matter and baryons. The potential is never able to decay as much as for $k = 0.3$/Mpc or $k = 0.05$/Mpc, so we do not get a point where $v'_{CDM} < 0$. And for large enough modes the horizon entry is so late that there are no baryon oscillations (horizon entry after decoupling). The $k = 0.0001$/Mpc mode is a good example of this.

As mentioned previously the photon temperature dipole $\Theta_1$ describes the photon velocity perturbation: $v_\gamma = -3\Theta_1$. For $k = 0.3$/Mpc it is clear that the curves for $\Theta_0$ and $\Theta_1$ are similar. The curve for $\Theta_1$ is shifted by a phase of $\frac{\pi}{2}$ relative to $\Theta_0$. That is of course because $\Theta_1$ describes the velocity of the photon density perturbations, and the velocity is zero when the density is at a maximum. Thus $\Theta_1 = 0$ when $\Theta_0$ has a maximum.

Figure 20 for $\Psi$ is very similar to Figure 19 for $\Phi$. This is because $\Psi \approx -\Phi$ is a good approximation[2]. This can be seen from equation (68). In the early universe the optical depth is very high, such that an electron interacts with photons from regions very nearby. And these nearby regions have quite similar temperature, such that the higher order multipoles will be almost negligible. So $\Theta_2$ is small, thus $\Psi \approx -\Phi$ in the early universe. And in the late universe $a \sim 1$, so the prefactor to $\Theta_2$ in (68) is quite small for the $k$'s we consider[3]. Thus $\Psi \approx -\Phi$ also in the late universe.

Of course, Figure 20 shows us that this can not be the whole story. $\Psi$ is not simply $-\Phi$. This is shown most clearly for $k = 0.0001$/Mpc. There is an upwards "bump" right after decoupling, which would not have been there had $\Psi = -\Phi$. The curve also slopes downwards until dark energy domination, and would have sloped upwards if $\Psi = -\Phi$. These differences are not nearly as apparent for $k = 0.3$/Mpc and $k = 0.05$/Mpc. That is because the prefactor in front of $\Theta_2$ in (68) goes as $k^{-2}$. So the fact that the discrepancy between $\Psi$ and $-\Phi$ is largest for the smallest $k$ is as expected.

Having looked at the details of how and why the perturbations on different scales evolve as they do we can now examine the general picture. The dark matter perturbations corresponding to the smallest scales enter the horizon first, so these perturbations will have more time to grow than the larger scales which enter the horizon later. The growth is, however, very suppressed during the radiation dominated era. Only when entering the matter dominated era do the perturbations grow significantly, in which case they grow approximately as $\delta_{CDM} \propto a$. The baryon perturbations are not allowed to grow before decoupling, because before that point they are bound to the photons. And since the photons oscillate due to the decaying potential the baryons will be forced along in the oscillation. Only when the baryons and photons decouple can the baryons move freely and fall into the potentials set up by the dark matter. The oscillation of baryons of course only applies to modes entering the horizon before decoupling, and especially those entering before matter-radiation equality, when the decay of the potential is significant. For modes that enter after decoupling the baryon density perturbation just follows the dark matter.

We also saw that the photon temperature multipole $\Theta_0$ is driven up by the decay of the potentials during radiation domination. And when the decay stops, the amplitude of $\Theta_0$ is damped due to photon diffusion. The smaller scale modes are the most damped, due to the damping factor $e^{-k^2/k_D^2}$. For the scales larger than $k \sim 0.3$/Mpc the amplitude is completely suppressed after decoupling, due to the increase in mean free path for the photons at that time. This will cause a visible effect on the CMB power spectrum - the larger $l$'s in the power spectrum will be suppressed due to this diffusion damping. And that is because the amplitude of $\Theta_0$ is very small around recombination due to this damping. However, $\Theta_0$ for the $k = 0.05$/Mpc mode is around a maximum at decoupling/recombination, so this mode will correspond to a maximum in the power spectrum[4]. The reason for this we come back to in the next milestone.

## 5. Milestone IV

In milestone I we computed the evolution of the background cosmological parameters, milestone II dealt with the recombination history of the universe and how the electron fraction and optical depth evolve in the universe. Milestone III then introduced perturbations to the previously smooth universe and integrated these perturbations forward in time to find how these depend on the time parameter $x$ and the Fourier wave number $k$. The CMB power spectrum is caused by these perturbations and how they propagate forward in time until today. So from all the ground

---

[2] Not at all times or for all modes, however.
[3] This is not actually true for $k = 0.0001$/Mpc, more on that in the next paragraph.

---

[4] The peak in the power spectrum is actually related to $\Theta_0 + \Psi$, so it is a bit more complicated than this. This is discussed in the next milestone

work done in the previous milestones we can now finally compute the CMB power spectrum.

## 5.1. Theory

Most of the theory section here is heavily inspired by Winther (2022d). Before we get to the actual integral for computing the power spectrum we need to discuss the $\Theta_\ell$'s from the previous milestone. We need $\Theta_\ell$ to compute $C_\ell$, and we want $\ell$ up to about 2000. So in principle one could then solve the system of differential equations for the perturbed quantities in milestone III with up to $\ell = 2000$. But that would be very computationally expensive. And luckily there is a trick called the line of sight integration (see Winther (2021)) which allows us to avoid this. The line of sight integral is given by

$$\Theta_\ell(k, x = 0) = \int_{-\infty}^{0} \tilde{S}(k, x) j_\ell[k(\eta_0 - \eta)] dx. \tag{86}$$

This allows us to evaluate any $\Theta_\ell$ by just knowing $\Theta_0, \Theta_2, \Psi, \Phi$ and $v_b$, as we will see below. Here $j_\ell(x)$ are the spherical Bessel functions. These take care of the transition from 3D to 2D, since the 3D perturbation field has to be projected onto a 2D spherical surface (the sky). These Bessel functions are explained in more detail in Winther (2021). The $\tilde{S}(k, x)$ is the so-called source function, and it is given by

$$\tilde{S}(k, x) = \tilde{g}\left[\Theta_0 + \Psi + \frac{1}{4}\Theta_2\right] + e^{-\tau}\left[\Psi' - \Phi'\right]$$

$$- \frac{1}{ck}\frac{d}{dx}(\mathcal{H}\tilde{g}v_b) + \frac{3}{4c^2k^2}\frac{d}{dx}\left[\mathcal{H}\frac{d}{dx}(\mathcal{H}\tilde{g}\Theta_2)\right]. \tag{87}$$

The first term in the source function is called the Sachs-Wolfe term. This is the dominant term, as we will see later. It is multiplied by the visibility function, which we learned in milestone II is highly peaked around recombination. So to a good approximation $\tilde{g}$ is a delta function around recombination, meaning the contribution to the line of sight integral from the first term is roughly

$$\Theta_\ell \approx (\Theta_0 + \Psi)_{\text{rec}} \, j_\ell(\eta_0),$$

where we have also neglected the quadrupole term because it is small, and the subscript "rec" signifies that the term should be evaluated at recombination. We have also neglected $\eta_{\text{rec}}$, because $\eta_{\text{rec}} \ll \eta_0$. So as a first approximation $\Theta_\ell$ is just $\Theta_0$ projected onto the sky by $j_\ell(k\eta_0)$, with a small correction due to the fact that the photons have to move out of the potential wells in which they are situated at recombination. The third term in $\tilde{S}$ is called the Doppler term. It is given in terms of the baryon velocity $v_b$, but in the early universe the photon velocity is equal to the baryon velocity. So this term describes the motion of the photons and how this causes a Doppler effect that influences $\Theta_\ell$. The second term in $\tilde{S}$ is the integrated Sachs-Wolfe effect, and it describes how photons gain energy when the potentials they move through decay over time. This effect is similar to the radiation driving effect that acts during radiation domination, but it only contributes after recombination. Before that point $\tau$ is huge, so the term is completely suppressed. After recombination this

term is basically just $\Psi' - \Phi'$. This term will thus only contribute during the late time dark energy domination, when the potentials decay again, and during a short period right after recombination. The last term in $\tilde{S}$ is not easy to give an intuitive explanation for. But it is also, as we will see, negligible compared to the three other terms. So $\Theta_\ell$ is to a good approximation produced by the monopole term at recombination, modified by having to climb out of potential wells, the Doppler effect due to the motion of the photon-baryon fluid at recombination, and the late time driving up of the amplitude of $\Theta_\ell$ due to decay of the potentials. Then all of this is multiplied by $j_\ell$ in order to project onto the sky.

The total temperature perturbation, $\Theta(\boldsymbol{x}, \hat{p}, t)$, at our position $\boldsymbol{x}$, in a direction $\hat{p}$ and at time $t$ (will be evaluated today) can be expanded in terms of the spherical harmonics $Y_{\ell m}(\hat{p})$.

$$\Theta(\boldsymbol{x}, \hat{p}, t) = \sum_{\ell=1}^{\infty} \sum_{m=-\ell}^{\ell} a_{\ell m}(\boldsymbol{x}, t) Y_{\ell m}(\hat{p}). \tag{88}$$

The $a_{\ell m}$'s are the spherical harmonics coefficients. These can be expressed as

$$a_{\ell m}(\boldsymbol{x}, t) = \int d\Omega_{\hat{p}} Y_{\ell m}^*(\hat{p}) \Theta(\boldsymbol{x}, \hat{p}, t), \tag{89}$$

where the integral is over all directions. $Y_{\ell m}*$ is the complex conjugate of $Y_{\ell m}$. The power spectrum can then be expressed as

$$C_\ell \equiv \langle |a_{\ell m}|^2 \rangle = \langle a_{\ell m} a_{\ell m}^* \rangle, \tag{90}$$

which is the expectation value of the $a_{\ell m}$. For theoretical calculations this is an ensemble average over many universes, while for practical computations we only have access to one universe. So the average is over all the $a_{\ell m}$'s corresponding to a given $\ell$. The number of $m$-values for a given $\ell$ is $2\ell + 1$, so for the low $\ell$'s this computed average will suffer from having too little data to compute an accurate average. So there is an inherent uncertainty in the lower $\ell$'s due to this, and it is called the cosmic variance problem.

$C_\ell$ can be rewritten as

$$C_\ell = 4\pi \int_0^\infty A_s \left(\frac{k}{k_{\text{pivot}}}\right)^{n_s - 1} \Theta_\ell^2(k) \frac{dk}{k}, \tag{91}$$

$n_s$ is the spectral index set up by inflation, and is related to how long inflation lasted. We will use $n_s = 0.96$. $A_s$ is the amplitude of the primordial perturbations at some scale $k_{\text{pivot}}$. We will use $A_s = 2 \cdot 10^{-9}$ for $k_{\text{pivot}} = 0.05/\text{Mpc}$. These three parameters are related to the primordial power spectrum, given by

$$\frac{k^3}{2\pi^2} P_{\text{primordial}}(k) = A_s \left(\frac{k}{k_{\text{pivot}}}\right)^{n_s - 1}. \tag{92}$$

All of this is explained in more detail in Winther (2021) and Winther (2022d). The primordial power spectrum enters the integral for $C_\ell$ due to the normalization scheme we chose in milestone III, where the initial condition for the curvature perturbation $\mathcal{R}$ is set to $\mathcal{R} = 1$. Keep in mind that the $\Theta_\ell$ defined in equation (88) is in terms of position in real space, whereas the $\Theta_\ell$ we have used otherwise, and also in equation (91) is in terms of Fourier coefficients in Fourier space.

With this in hand we can now compute the power spectrum, $C_\ell$ for all the $\ell$'s we want by first performing the line of sight integral for the $\ell$'s we want to consider.

We also want to compute the so-called matter power spectrum. This is given by

$$P(k, x) = |\Delta_M(k, x)|^2 P_{\text{primordial}}(k), \tag{93}$$

where

$$\Delta_M(k, x) \equiv \frac{c^2 k^2 \Phi(k, x)}{\frac{3}{2}\Omega_{M0}a^{-1}H_0^2}. \tag{94}$$

is the gauge invariant density perturbation.

## 5.2. Implementation details

In all the following computations, when calculating $j_\ell(x)$, $\Theta_\ell$ and $C_\ell$ we do so for 63 different values of $\ell$ in the range $\ell = \{2, 2000\}$. The results are then splined.

In order to calculate the line of sight integral, we need the spherical Bessel function. We use the GSL library to calculate $j_\ell(z)$ for the $\ell$'s specified above, and for $z \in \{0, k_{\max}\eta_0\}$, with $k_{\max} = 0.3$ Mpc$^{-1}$ being the maximum wavenumber used for computing the perturbations. The Bessel function is an oscillating function with period of $2\pi$, so in order to sample it appropriately we need to include multiple samples per oscillation. Here we will use $n = 16$ samples per oscillation, such that the difference between samples is $\Delta z = \frac{2\pi}{n}$. With our $\eta_0 \approx 1.4 \cdot 10^4$ Mpc we get around 11000 samples (with $z_{\max} = k_{\max}\eta_0$). The result can then be splined to allow for calling the Bessel function for any $j_\ell$ and $z$ without having to access the GSL library all the time.

We also need the source function to compute the line of sight integral. All the quantities in the source function are computed in previous milestones. When we need derivatives of known quantities we use numerical differentiation on the splines we already have. The source function is a slowly varying function of $k$ and $x$ except around decoupling. So we do not need as many samples for our spline. Here we use 1000 logarithmically spaced $k$-values between $k_{\min} = 5 \cdot 10^{-5}$ Mpc$^{-1}$ and $k_{\max} = 0.3$ Mpc$^{-1}$. And we use 1000 linearly spaced $x$-values between $\log\left(10^{-8}\right)$ and 0. Then the results are splined, using a 2D spline in $k$ and $x$.

In order to compute $\Theta_\ell$ we need to sample the integrand of (86) and perform a numerical integration. The integral is over $x$, but

we need to compute it for many values of $k$ (and $\ell$). The resolution in both $k$ and $x$ thus has to high enough to produce accurate results. Here we use 2000 linearly spaced $k$-values between the same $k_{\min}$ and $k_{\max}$ as before. And 1000 linearly spaced $x$-values in the same range as before. These number of $k$- and $x$-samples were simply chosen through trial and error. With these samples in hand we can then perform a numerical integration, and we could use any scheme we wanted. Here we use the trapezoidal rule, which can be written as

$$\int_a^b f(x)dx \approx \frac{\Delta x}{2} \left[ f(a) + 2f(a + \Delta x) + ... + 2f(b - \Delta x) + f(b) \right], \tag{95}$$

where $\Delta x$ is the separation between the sample points. For this form of the trapezoidal rule to be valid the samples need to be linearly spaced, which they are in our case. After performing this integral for all the $k$-values and $\ell$-values we spline the result in $k$.

Finally we can compute the power spectrum $C_\ell$. $\Theta_\ell$ is an integral over the source function (times $j_\ell$), which contains the visibility function. The source function will thus be peaked around recombination, and $\Theta_\ell$ can therefore be approximated as

$$\Theta_\ell \approx j(k\eta_0) \int_{-\infty}^0 \tilde{S}(k, x)\,dx \propto j_\ell(k\eta_0) \tag{96}$$

because $\eta_0 \gg \eta$ for $\eta = \eta(x_{\text{rec}})$. Therefore the power spectrum can be approximated as

$$C_\ell \propto \int_0^\infty k^{n_s-1} \frac{j_\ell^2(k\eta_0)}{k} dk \tag{97}$$

The Bessel function having oscillations with period $2\pi$ thus means the integrand of $C_\ell$ will have oscillations of period $\Delta k = \frac{2\pi}{\eta_0}$. So if we want to sample the integrand $n$ times per oscillation we need to have $\Delta k = \frac{2\pi}{n\eta_0}$. This short discussion is taken from Callin (2006). Here we choose $n = 32$. The integral is then computed numerically, again using the trapezoidal rule. The result can then be splined in $\ell$.

Again these computations are very suited for being parallelized. All the different $\ell$'s are independent, so the computations of $j_\ell$, $\Theta_\ell$ and $C_\ell$ can all be parallelized over $\ell$.

## 5.3. Results

We compute the spline for the spherical Bessel functions $j_\ell$ and for the source function. Then we use this to compute the $\Theta_\ell$'s, which in turn are splined and used to compute the $C_\ell$'s. In much of the discussion that follows we will use the term "scale" loosely, referring both to physical scale characterized by $k$ and angular scale characterized by $\ell$. But these two are closely related due to the rough approximation that features on physical scale $k$ correspond to features on angular scale $\ell$. So when referring simply to "scale" the meaning should be clear from context. We will justify this correspondence between $k$ and $\ell$ shortly. First

of all we now plot $\Theta_\ell$ for $\ell = 10, 100$ and 1000 as functions of $k$ to work towards seeing how the integrand of (91) behaves. Figure 21 shows this. The $x$-axis is here in units of $c/H_0$ for more handy numbers, and in logarithmic scale.
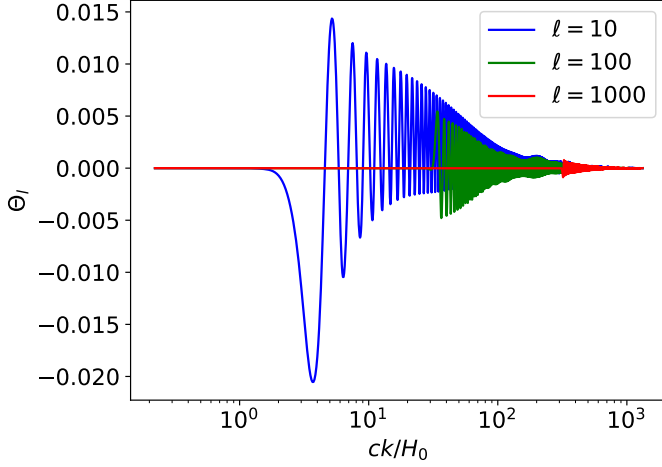


**Fig. 21.** Plot showing $\Theta_\ell(k)$ for $\ell = 10, 100$ and 1000. The $x$-axis is plotted in units of $c/H_0$ for more manageable numbers, and in logarithmic scale. The $y$-axis of course shows the value of $\Theta_\ell$. Clearly these three $\Theta_\ell$'s peak at different $k$'s and then gradually fall off with increasing $k$. Before the peak they are close to zero.

Consider now only the first term, the Sachs-Wolfe term, in the integrand in the expression for $\Theta_\ell$ (neglecting the quadrupole). Then, very roughly, $\Theta_\ell$ is given by

$$\Theta_\ell(k, x = 0) \approx (\Theta_0 + \Psi)_{\text{rec}} \, j_\ell(k\eta_0). \tag{98}$$

The spherical Bessel function $j_\ell(z)$ is peaked around $z = \ell$. For the three values of $\ell$ the peak is then around $ck/H_0 = 3.2, 32$ and 320 respectively, for $\ell = 10, 100$ and 1000. And since $\Theta_\ell$ is roughly proportional to $j_\ell(k\eta_0)$ we would then also expect it to be peaked around these three values for the three $\ell$'s (this discussion is inspired by the very similar discussion in Winther (2021)). From Figure 21 we see that this is indeed the case, but the peaks are not sharp. The decay as $k$ increases away from the peak is very slow. This comes from the fact that the Bessel functions are not really very peaked, they decay very slowly. But for $k \lessgtr \ell/\eta_0$ it is close to zero, which is why $\Theta_\ell$ is also approximately zero before the peak.

It is a useful approximation to assume $\Theta_\ell$ is only non-zero at $k = \ell/\eta_0$, because this means that the contribution to the integral in the expression for $C_\ell$ only comes from $\Theta_\ell(k = \ell/\eta_0, x = 0)$. And thus we can say that the features in the power spectrum at an angular scale $\ell$ correspond to modes of physical scale $k = \ell/\eta_0$. Figure 21 shows that this must be taken with a grain of salt, however, since there are also significant contributions from higher $k$. But the integrand in (91) goes as $\Theta_\ell^2/k$ (for our $n_s = 0.96$, which is close to 1), so $\Theta_\ell^2$ will be more peaked, and the additional factor $1/k$ also contributes to suppressing larger $k$. So the approximation is not as bad as it looks from Figure 21, but must not be taken too literally. This last point can be demonstrated by plotting $\Theta_\ell^2/k$ as a function of $k$ for the same three values of $\ell$.

Figure 22 shows this. The $x$-axis is again in units of $c/H_0$, and the $y$-axis is in units of $H_0/c$. Both axes are logrithmic.
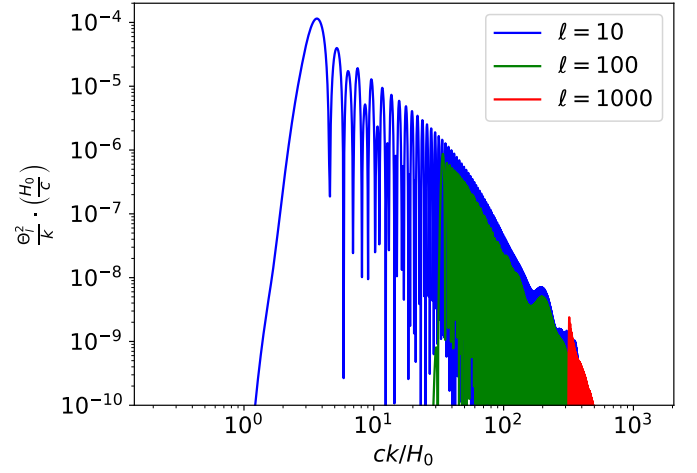


**Fig. 22.** Plot of the integrand in the expression for $C_\ell$ for the same three values of $\ell$ as earlier, $\ell = 10, 100$ and 1000. This is not exactly correct, since we have neglected the factor $A_s \left( \frac{k}{k_{\text{pivot}}} \right)^{n_s - 1}$. But since $n_s - 1 = -0.04$ this will be approximately constant. The $x$-axis in the plot is again in units of $c/H_0$, while the $y$-axis is now $\Theta_\ell^2/k$ in units of $H_0/c$. Both axes are now in logaritmhic scale.

Clearly the integrand of $C_\ell$ peaks for $k \approx \ell/\eta_0$, and then decays. Keep in mind that the $y$-axis is logarithmic, so the contributions from higher $k$ become negligible quite quickly. $C_\ell$ is thus given by $C_\ell \propto \Theta_\ell^2(k = \ell/\eta_0, x = 0)/k$ to a decent approximation, with corrections from the slightly higher $k$ that contribute a bit. Having looked at the integrand of $C_\ell$ we can then look at the actual $C_\ell$'s. The power spectrum is plotted in Figure 23. The $x$-axis gives the multipole $\ell$ and is logarithmic. And the $y$-axis represents $\frac{\ell(\ell+1)}{2\pi} C_\ell T_{\text{CMB0}}^2$ in $\mu K^2$. The red curve shows our theoretical prediction of the power spectrum while the points with error bars are the data points from Planck 2018.
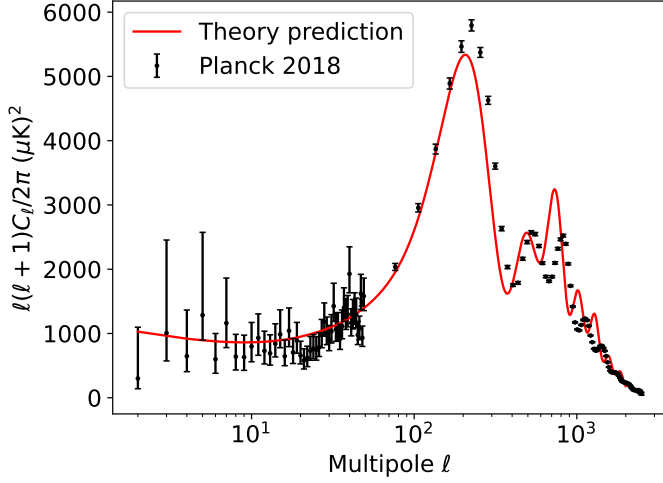
**Fig. 23.** Plot showing the power spectrum of the CMB as computed from our treatment of the evolution of the perturbations. The red curve represents our theoretical prediction, while the black points with error bars are data points from Planck 2018. The $x$-axis represents multipole $\ell$ on a logarithmic scale, while the $y$-axis represents $\frac{\ell(\ell+1)}{2\pi}C_\ell T^2_{\text{CMB0}}$ in $\mu K^2$. The fit between our prediction and the data is decent at low $\ell$, but there are clearly discrepancies at larger $\ell$, starting around the first peak at $\ell \sim 200$.

Clearly the agreement between our prediction and the data is good at small $\ell$. But for $\ell$ around the first peak, $\ell \sim 200$, and higher the results do not agree more than just very roughly. The observations clearly show a higher first peak, which is also at somewhat higher $\ell$, than our model predicts. Additionally the second and third peaks from the observations are approximately the same height. That is not the case in our model, which predicts that the third peak should be significantly higher than the second peak. We also see that the second and third peaks are at slightly higher $\ell$'s in the data from the observations. But these discrepancies are simply because we have not included neutrinos and polarization in our model. Neutrinos will contribute significantly to the radiation energy density, and also have perturbations of their own that contribute to the gravitational potentials. Polarization will also influence $\Theta_2$ and the source function, so it is not surprising that we do not get totally accurate results when neglecting neutrinos and polarization. Our prediction does get the general features correct, however. There are a set of peaks, a Sachs-Wolfe plateau at low-$\ell$ and a damping for higher $\ell$'s. These higher $\ell$'s correspond to small angular scales, which are so small that the diffusion damping effect damps these scales (like we discussed in milestone III).

Despite neglecting neutrinos and polarization the power spectrum that we have computed does exhibit an expected shape. Before we study how the power spectrum depends on the cosmological parameters we will look into the four different terms in the source function and examine how these contribute to the power spectrum. Figure 24 shows this. The $x$- and $y$-axes are the same as in Figure 23. The blue curve represents the first term in (87), the Sachs-Wolfe term. The red curve is the second, ISW, term, the dashed green curve is the Doppler term. And the dotted magenta curve represents the fourth term.
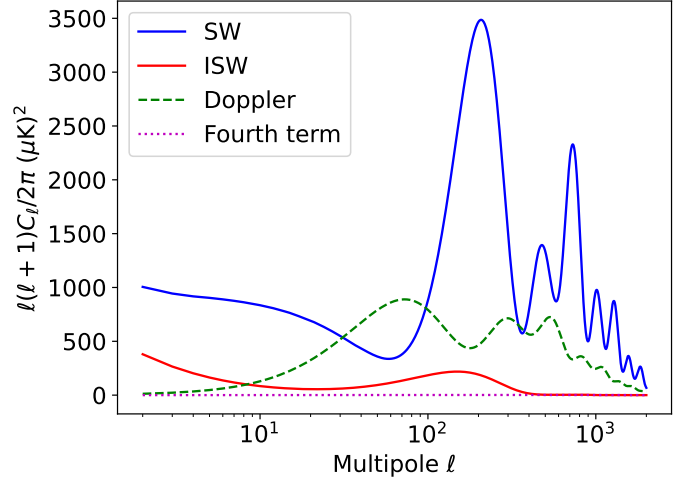


**Fig. 24.** Plot showing the contributions to the power spectrum from the four terms in the source function. The blue curve represents the contribution from the Sachs-Wolfe term, the red curve is for the integrated Sachs-Wolfe term, the dashed green curve is the Doppler term, while the dotted magenta curve is the last term in the source function. The $x$-axis is again logarithmic and represents the multipole $\ell$. The $y$-axis represents $\frac{\ell(\ell+1)}{2\pi}C_\ell T^2_{\text{CMB0}}$ in $\mu K^2$. Clearly the SW term dominates, with a significant contribution from the Doppler term, and a much smaller contribution from the ISW term. The contribution from the last term in the source function is negligible.

As stated in the theory section the Sachs-Wolfe term dominates and is the largest contribution to the power spectrum. It exhibits the main features of the power spectrum, the peaks and roughly their relative heights. And this is to be expected, since the Sachs-Wolfe term is the term involving $\Theta_0$ and we know (see Winther (2021) for example) that the peaks in the power spectrum correspond to the peaks in sound waves travelling through the universe before recombination. The peaks correspond to the scales that are such that $\Theta_0$ is at a maximum at recombination. So this term is expected to exhibit the characteristic peaks in the power spectrum. But the so-called Sachs-Wolfe plateau has a dip and is much steeper than in the actual power spectrum. The second most important term is clearly the Doppler term. First off, it is clear that this term does not contribute to the largest scale. And that is because the largest scales have only entered the horizon in the late universe, at which point the visibility function is basically zero. Thus the whole term is roughly zero. The Doppler term is, however, important for larger $\ell$'s - corresponding to smaller scales. At scales that enter the horizon before matter-radiation equality the baryon velocity will be oscillating before decoupling, as is shown in Figure 17 in milestone III. So different scales will be frozen out with different baryon velocities, which will cause the Doppler term to oscillate with scale. This is what we see in Figure 24.

The next term is the integrated Sachs-Wolfe term. This term describes how the source function, and thus also the multipoles, are driven up by the decay of the potentials after decoupling. Right after decoupling the potentials are still decaying somewhat for the modes of intermediate scale. For the very small scale modes, like $k = 0.3$ Mpc$^{-1}$ in Figure 19, the potential does not decay after decoupling, because it has already decayed practically to zero during radiation domination. And for the largest scales, like $k = 0.0001$ Mpc$^{-1}$, the potentials also do not decay right after decoupling, but here because these scales are still

outside the horizon. For intermediate scales the potential can still decay right after decoupling. And for both intermediate and large scales the potential will start decaying again during dark energy domination. This decay will be most dramatic for the largest scales, as can be seen from Figure 19. These decays are shown in the curve for the ISW term in Figure 24. For the largest scales (small $\ell$) the only contribution is from the late time decay of the potentials during dark energy domination. And for slightly smaller scales the decay is less dramatic, so the contribution to the ISW term from the late time decay is smaller. But for intermediate scales the early time ISW due to the still slightly decaying potentials right after decoupling also contribute. And for small scales the potentials have already decayed to zero during radiation domination, so neither of these decays after decoupling occur for small scales. Hence the shape of the curve for the ISW term. The last term in the source function is the dashed magenta curve. Clearly it is totally negligible for all scales. This is not too surprising. The visibility function means it will roughly only get contributions from recombination to decoupling. And at these times the quadrupole, $\Theta_2$, is still quite small.

Having explored the different terms contributing to the power spectrum we can now study how the power spectrum changes when we change some of the cosmological parameters. This requires precision in how we define the changes in the parameters. We could for example change $\Omega_{\Lambda0}$ while keeping $h$ constant, but since $\Omega_{m0} + \Omega_{\Lambda0} = 1$ (neglecting radiation for now) in a flat universe this means we are also changing $\Omega_{m0}$ at the same time. We will consider three changes of parameters. These will be

– Change $\Omega_{\Lambda0}$ and keep $\Omega_{m0}h^2$ constant
– Change $\Omega_{m0}$ and keep $\Omega_{\Lambda0}h^2$ and $\Omega_{b0}h^2$ constant
– Change $\Omega_{b0}$ and keep $\Omega_{m0}$ (and thus also $\Omega_{\Lambda0}$) constant

This of course means $h$ will have to change as well (in the first two cases). The exact manner in which these changes are performed is discussed in Appendix C. Figure 25 shows the power spectra for the models with these changes introduced, together with the power spectrum for the fiducial model. The $x$- and $y$-axes are the same as before. The blue curve is for the fiducial model, the red curve is for the model with $\Omega_{\Lambda0}$ being changed to $\Omega_{\Lambda0} = 0.9$. The dashed green curve is with a change in $\Omega_{m0}$, $\Omega_{m0} = 0.5$ and the dotted magenta curve is with a change in $\Omega_{b0}$, $\Omega_{b0} = 0.1$.
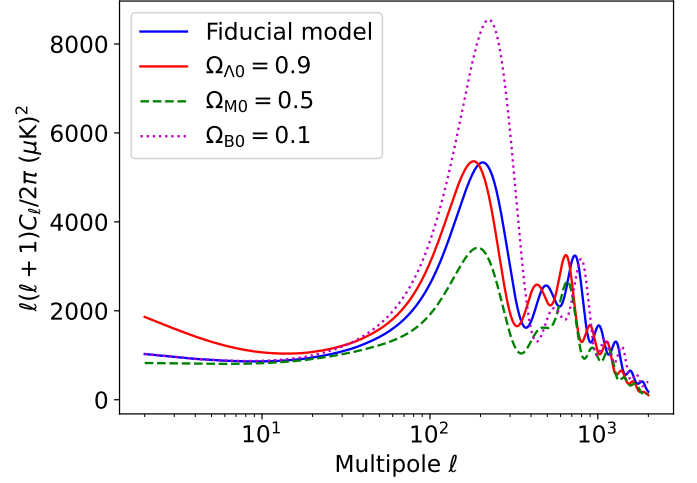


**Fig. 25.** Plot of the power spectra where we have changed cosmological parameters. The blue curve represents the fiducial model. The red curve is for $\Omega_{\Lambda0} = 0.9$ with $\Omega_{m0}h^2$ constant. The dashed green curve is for $\Omega_{m0} = 0.5$ with $\Omega_{\Lambda0}h^2$ and $\Omega_{b0}h^2$ constant. The dotted magenta curve is for $\Omega_{b0} = 0.1$ with $\Omega_{m0}$ and $\Omega_{\Lambda0}$ constant. The $x$- and $y$-axes are the same as before. Clearly the power spectrum changes when changing the cosmological parameters. How it changes depends on which parameter we change.

Consider first the curve for $\Omega_{\Lambda0} = 0.9$. This is very similar to the fiducial curve. Apart from the Sachs-Wolfe plateau the height of the spectrum is left unchanged, the whole spectrum is simply shifted towards lower $\ell$'s. This change is due to the change in the comoving distance to the last scattering surface, $\eta_0 - \eta_{rec}$. When increasing $\Omega_{\Lambda0}$ while keeping $\Omega_{m0}h^2$ constant then the comoving distance to the last scattering surface decreases. $\ell$ is proportional to this comoving distance (and inversely proportional to the sound horizon, but this varies slowly) so decreasing $\eta_0 - \eta_{rec}$ causes a decrease in $\ell$. Hence why the whole power spectrum shifts toward lower $\ell$. As mentioned earlier the Sachs-Wolfe plateau also changes significantly. For the lowest $\ell$, corresponding to the largest angular scales, $C_\ell$ is significantly higher for $\Omega_{\Lambda0} = 0.9$ than for the fiducial model. This is due to the ISW effect. We saw earlier that the late time ISW effect during dark energy domination caused the potentials for very large scale modes to decay dramatically. Increasing $\Omega_{\Lambda0}$ means matter-radiation equality will occur earlier, allowing the potentials to decay for longer. And so the power spectrum for large scale modes is even more driven up. The rough correspondence $\ell \sim k\eta_0$ then roughly maps these large scale modes to small $\ell$, explaining the change in the Sachs-Wolfe plateau.

The dashed green curve is for $\Omega_{m0} = 0.5$. Clearly this power spectrum is much lower than the fiducial one. Intermediate to small scale modes enter the horizon during radiation domination, and their potentials then decay. This drives $\Theta_0$, and thus also $C_\ell$ (again due to $\ell \sim k\eta_0$) up for these scales. But when increasing $\Omega_{m0}$ we push back matter-radiation equality to earlier times. This means the potentials will have less time to decay, so the radiation driving effect will not be as strong. The largest scales are still outside the horizon during matter-radiation equality, so these will not be influenced by the radiation driving during radiation domination. This is why the high-$\ell$ part of the power spectrum is lowered by increasing $\Omega_{m0}$ while the Sachs-Wolfe plateau is not. That is not completely true, because we see that the plateau

is somewhat lowered on the largest angular scales. The reason for that change is that increasing $\Omega_{m0}$ means $\Omega_{\Lambda0}$ is smaller, so matter-dark energy equality is later than in the fiducial model. So the late time ISW effect has less time to drive up the power spectrum. As discussed earlier that effect is most important for the largest scales (lowest $\ell$'s), and thus the power spectrum for the lowest $\ell$'s is slightly lowered when increasing $\Omega_{m0}$. Another small detail is that the peaks are again slightly shifted to lower $\ell$. This is again because the comoving distance to the last scattering surface is slightly lowered.

The last change we have performed is setting $\Omega_{b0} = 0.1$. Now we clearly see that the first peak is much higher than in the fiducial model. The third peak is also enhanced relative to the second peak. This is because of the so-called baryon loading effect. A pure photon fluid would just want to oscillate symmetrically around $\Theta_0 = 0$. But as we add baryons these will be dragged along with the photons in the early universe. But they will also want to collapse. So when the fluid consisting of photons and baryons starts oscillating the baryons will tend to cause the fluid to compress tightly, and then will try to slow down the rarefaction. This means the highest overdensity will be higher than for a pure photon fluid, and the lowest overdensity will also be higher than for a photon fluid. So the oscillations in overdensity will be asymmetric around zero. And since the integrand of $C_\ell$ is proportional to $\Theta_\ell^2$ all the peaks will be positive, but the baryon loading effect causes the even peaks to be lower than the odd peaks. And this is why the first peak is driven up and the third peak is enhanced relative to the second peak. As before this effect also only affects scales that are inside the horizon before matter-radiation equality. Hence why the largest scales are unchanged. It is also clear (especially from the third peak) that the power spectrum when increasing $\Omega_{b0}$ is shifted to the right, towards higher $\ell$. We required that $\Omega_{m0}$ and $\Omega_{\Lambda0}$ should be constant, so the comoving distance to the last scattering surface is not changed. But since the photons and baryons travel together during radiation domination the sound speed of the fluid depends on how much baryons there are. When increasing the amount of baryons the photons have to carry with them more baryons, so the sound speed is lowered. Then the sound horizon is also lowered, which causes the power spectrum to be shifted towards higher $\ell$ (smaller scales).

We have also plotted a realization of a map of the CMB as it could look given our model. This is done by picking $a_{\ell m}$'s pseudo-randomly from Gaussian distributions with variance $\frac{C_\ell}{\sqrt{2}}$, as is explained in Winther (2021). The temperature perturbation as a function of direction on the sky is then given by the $a_{\ell m}$'s together with spherical harmonics, as in (88). Figure 26 shows this map, with the monopole and dipole subtracted off. These are subtracted because they are much larger than the subsequent multipoles, so it is just to be able to see details. Clearly it looks quite similar to the map of the Planck 2018 observational data. Of course the exact map is random, we are not able to predict exactly how the real map of the CMB looks, just its statistical behavior. So we should not expect our map to exactly match the Planck 2018 map anyway. But it is also important to keep in mind that we know that our power spectrum deviated from the observations for around the first peak and higher. So we should expect the map we predict to be slightly different than the observations for angular scales smaller than around $\ell = 200$ (the first peak).
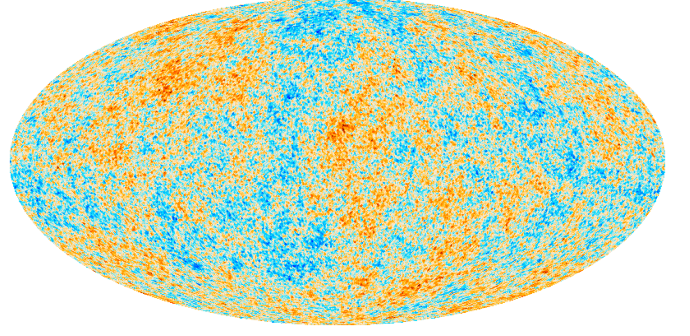


**Fig. 26.** A realization of a map of the CMB as it could look with the power spectrum we have computed. The monopole and dipole are subtracted off.

The CMB power spectrum that we have studied now roughly describes the dependence of the $\Theta_\ell$'s on scale $k$ (since we have the rough map $k \sim \ell/\eta_0$. And although the CMB power spectrum depends on the matter perturbations we also want to see explicitly how the matter density perturbations depend on scale. We therefore also compute and plot the matter power spectrum. Figure 27 shows this. Both axes are on logarithmic scale. The $x$-axis is in units of $h/$Mpc, while the $y$-axis is in units of $(\text{Mpc}/h)^3$. The red curve represents the computed spectrum for the fiducial model, while the points with error bars again indicate data points, this time from SDSS DR7 LRG surveys. The dashed vertical line indicates $k_{\text{eq}} = \frac{\mathcal{H}(a_{\text{eq}})}{c}$, which is the wavenumber of the scale that enters the horizon at matter-radiation equality. As we have seen before, whether or not a scale enters the horizon before or after matter-radiation equality is important for how it evolves.
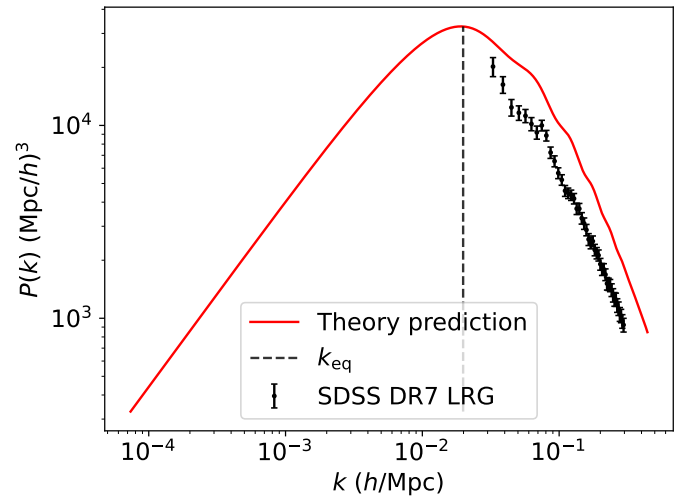


**Fig. 27.** The matter power spectrum as a function of scale $k$. The red curve gives the theoretical prediction while the points with error bars are observational data from SDSS DR7 LRG surveys. The dashed vertical line indicates where $k = k_{\text{eq}}$, the scale which enters the horizon at matter-radiation equality. Clearly the matter power spectrum increases for $k < k_{\text{eq}}$ and decreases for $k > k_{\text{eq}}$. The $x$-axis is in units of $h/$Mpc, while the $y$-axis is in units of $(\text{Mpc}/h)^3$

There is a clear increase in the matter power spectrum for $k < k_{eq}$, while it decreases for $k > k_{eq}$. The turning point is clearly $k = k_{eq}$, which is not coincidental. More on that shortly. Our prediction again falls short of the observational data. But this is, as for the CMB power spectrum, because we have not included neutrinos and polarization. The general trend for $k > k_{eq}$ is, however, nicely captured in both the data and our theoretical prediction.

The small modes, with $k > k_{eq}$, enter the horizon before matter-radiation equality. As explained in Winther (2021) $P(k)$ of scales entering the horizon before matter-radiation equality will be suppressed by a factor $\left(\frac{k_{eq}}{k}\right)^4$ relative to their growths if they did not enter the horizon before matter-radiation equality. Otherwise they would have grown as $k^{n_s} \sim k$, so the small scale part of the matter power spectrum should go as $k^{-3}$. The reason for the suppression is just that perturbations are not allowed to grow during radiation domination, they are frozen until matter domination. The large scale modes, with $k < k_{eq}$, will not experience this suppression, because they enter the horizon after matter-radiation equality. And so they will simply grow as $k^{n_s}$ at all times. The fact that the power spectrum goes as $k^{n_s} \sim k$ for $k < k_{eq}$ is just a consequence of the primordial power spectrum.

## 6. Conclusions

We have computed the power spectrum of the CMB by solving for the background cosmology, recombination history and evolution of density and velocity perturbations on top of a smooth background. Our model neglects neutrinos and polarization, so there is a discrepancy between our model and the power spectrum inferred by the Planck 2018 observational data of the CMB. But our model does produce a qualitatively quite correct power spectrum. We get the expected acoustic peaks from sound waves prior to recombination, the first peak is the dominant one, the diffusion damping is evident and the Sachs-Wolfe plateau is clearly present. The fact that it is qualitatively correct was further demonstrated by changing some of the cosmological parameters, $\Omega_{\Lambda 0}$, $\Omega_{m0}$ and $\Omega_{b0}$, and studying how this changes the power spectrum. The results were as expected from a qualitative understanding of effects like baryon loading and radiation driving. From our exploration of the evolution of the perturbations we have also seen how the peaks in the CMB power spectrum can be traced back to sound waves in the early universe, before recombination. It is clear that our model here is not able to achieve anything close to the accuracy of CMBFAST, for instance, without including neutrinos and polarization. So this is definitely the next step in improving the work done here. A lot of work can also be done to optimize the program used to compute the power spectrum. It runs in 20-30 seconds on a slightly below average laptop (2022), which would be too slow to perform a parameter estimation from the CMB.

## References

Baumann, D. 2015, Cosmology
Callin, P. 2006
Dodelson, S. 2011, Modern Cosmology
Valentino, E. D. 2021
Winther, H. A. 2021, Cosmology II - Lecture notes, `https://cmb.wintherscoming.no/literature.php`
Winther, H. A. 2022a, Milestone I, `https://cmb.wintherscoming.no/milestone1.php`
Winther, H. A. 2022b, Milestone II, `https://cmb.wintherscoming.no/milestone2.php`
Winther, H. A. 2022c, Milestone III, `https://cmb.wintherscoming.no/milestone3.php`
Winther, H. A. 2022d, Milestone IV, `https://cmb.wintherscoming.no/milestone4.php`
Øystein Elgarøy. 2021, Lecture notes AST3220

## Appendix A: Background cosmology

*Appendix A.1: Derivatives of $H$ and $\mathcal{H}$ wrt. $x$*

In these derivations we will define $\Omega_{m0} = \Omega_{b0} + \Omega_{\mathrm{CDM0}}$ and $\Omega_{r0} = \Omega_{\gamma0} + \Omega_{\nu0}$. Then

$$H = H_0 \sqrt{\Omega_{m0}a^{-3} + \Omega_{r0}a^{-4} + \Omega_{\Lambda0}}, \tag{A.1}$$

where we have neglected $\Omega_{k0}$, because it will be zero throughout this paper. Let us first find $\frac{dH}{da}$:

$$\frac{dH}{da} = \frac{H_0}{2\sqrt{\Omega_{m0}a^{-3} + \Omega_{r0}a^{-4} + \Omega_{\Lambda0}}} \cdot \left[ -3\Omega_{m0}a^{-4} - 4\Omega_{r0}a^{-5} \right] \tag{A.2}$$

$$= -\frac{H_0^2}{2H} \left[ 3\Omega_{m0}a^{-4} + 4\Omega_{r0}a^{-5} \right] \tag{A.3}$$

Then the first derivatives of $H$ and $\mathcal{H}$ wrt. $x$ are

$$\frac{dH}{dx} = \frac{da}{dx}\frac{dH}{da} = a\frac{dH}{da} \tag{A.4}$$

$$\frac{d\mathcal{H}}{dx} = \frac{d(aH)}{dx} = H\frac{da}{dx} + a\frac{dH}{dx} = aH + a\frac{dH}{dx} \tag{A.5}$$

$$= \mathcal{H} + a\frac{dH}{dx} \tag{A.6}$$

because $\frac{da}{dx} = a$. For the second derivatives wrt. $x$ we first need to find $\frac{d^2H}{da^2}$.

$$\frac{d^2H}{da^2} = -\frac{H_0^2}{2}\left[ \frac{d}{da}\left(\frac{1}{H}\right)\left(3\Omega_{m0}a^{-4} + 4\Omega_{r0}a^{-5}\right) \right. \tag{A.7}$$

$$\left. + \frac{1}{H}\frac{d}{da}\left(3\Omega_{m0}a^{-4} + 4\Omega_{r0}a^{-5}\right) \right] \tag{A.8}$$

$$= \frac{H_0^2}{2}\left[ \frac{1}{H^2}\frac{dH}{da}\left(3\Omega_{m0}a^{-4} + 4\Omega_{r0}a^{-5}\right) \right. \tag{A.9}$$

$$\left. + \frac{1}{H}\left(12\Omega_{m0}a^{-5} + 20\Omega_{r0}a^{-6}\right) \right] \tag{A.10}$$

The second derivatives wrt. $x$ are then

$$\frac{d^2H}{dx^2} = \frac{da}{dx}\frac{d}{da}\left(a\frac{dH}{da}\right) = a\left(\frac{dH}{da} + a\frac{d^2H}{da^2}\right) \tag{A.11}$$

$$\frac{d^2\mathcal{H}}{dx^2} = \frac{d}{dx}\left(\mathcal{H} + a\frac{dH}{dx}\right) \tag{A.12}$$

$$= \frac{d\mathcal{H}}{dx} + \frac{da}{dx}\frac{dH}{dx} + a\frac{d^2H}{dx^2} \tag{A.13}$$

$$= \frac{d\mathcal{H}}{dx} + a\frac{dH}{dx} + a\frac{d^2H}{dx^2} \tag{A.14}$$

Since we already have the expressions for $\frac{d\mathcal{H}}{dx}$ etc. there is no need to find explicit expressions for $\frac{d^2H}{dx^2}$, and $\frac{d^2\mathcal{H}}{dx^2}$.

*Appendix A.2: Value of $\frac{1}{\mathcal{H}}\frac{d\mathcal{H}}{dx}$ in different regimes*

A good test for $\frac{1}{\mathcal{H}}\frac{d\mathcal{H}}{dx}$ as a function of $x$ is to compare with analytical values in radiation, matter and dark energy domination respectively. I will now introduce a notation $\Omega(a)$ which just represents the sum of the density parameters (in matter + radiation domination $\Omega(a) = \Omega_{m0}a^{-3} + \Omega_{r0}a^{-4}$, for instance). The general analytical form is

$$\frac{1}{\mathcal{H}}\frac{d\mathcal{H}}{dx} = \frac{1}{\mathcal{H}}\left(\mathcal{H} + a\frac{dH}{dx}\right) = 1 + \frac{1}{H}\frac{dH}{dx} \tag{A.15}$$

$$= 1 + \frac{1}{H_0\sqrt{\Omega(a)}}\frac{H_0}{2\sqrt{\Omega(a)}}\frac{da}{dx}\frac{d\Omega(a)}{da} \tag{A.16}$$

$$= 1 + \frac{a}{2\Omega(a)}\frac{d\Omega(a)}{da} \tag{A.17}$$

because $H = H_0\sqrt{\Omega(a)}$. In radiation domination $\Omega(a) = \Omega_{r0}a^{-4}$, so $\frac{d\Omega(a)}{da} = -4\Omega_{r0}a^{-5}$, meaning

$$\frac{1}{\mathcal{H}}\frac{d\mathcal{H}}{dx} = 1 + \frac{1}{2}a\cdot\frac{a^4}{\Omega_{r0}}\left(-4\Omega_{r0}a^{-5}\right) = 1 - 2 = -1. \tag{A.18}$$

In matter domination $\Omega(a) = \Omega_{m0}a^{-3}$, so $\frac{d\Omega(a)}{da} = -3\Omega_{m0}a^{-4}$, meaning

$$\frac{1}{\mathcal{H}}\frac{d\mathcal{H}}{dx} = 1 + \frac{1}{2}a\cdot\frac{a^3}{\Omega_{m0}}\left(-3\Omega_{m0}a^{-4}\right) = 1 - \frac{3}{2} = -\frac{1}{2}. \tag{A.19}$$

And, finally, in dark energy domination $\Omega(a) = \Omega_{\Lambda0}$, so $\frac{d\Omega(a)}{da}) = 0$, meaning

$$\frac{1}{\mathcal{H}}\frac{d\mathcal{H}}{dx} = 1 + \frac{1}{2}\frac{1}{\Omega_{\Lambda0}}\cdot 0 = 1 \tag{A.20}$$

*Appendix A.3: Value of $\frac{1}{\mathcal{H}}\frac{d^2\mathcal{H}}{dx^2}$ in different regimes*

As for $\frac{1}{\mathcal{H}}\frac{d\mathcal{H}}{dx}$ it is also a good test for the second derivative to compare with analytical values in the different regimes. We already know that

$$\frac{d^2\mathcal{H}}{dx^2} = \frac{d\mathcal{H}}{dx} + a\frac{dH}{dx} + a\frac{d^2H}{dx^2}$$

$$= aH + 2a\frac{dH}{dx} + a\frac{d^2H}{dx^2},$$

so we need expressions for $\frac{dH}{dx}$ and $\frac{d^2H}{dx^2}$. With $H = H_0\sqrt{\Omega}$ we get

$$\frac{dH}{dx} = \frac{H_0}{2\sqrt{\Omega}}\frac{d\Omega}{dx},$$

and

$$\frac{d^2H}{dx^2} = -\frac{H_0}{4\Omega^{3/2}}\left(\frac{d\Omega}{dx}\right)^2 + \frac{H_0}{2\sqrt{\Omega}}\frac{d^2\Omega}{dx^2}$$

And it is easier to work with $\frac{d\Omega}{dx}$ here, rather than $\frac{d\Omega}{da}$, so we will stick to that here. Then

$$\frac{1}{\mathcal{H}}\frac{d^2\mathcal{H}}{dx^2} = \frac{1}{\mathcal{H}}\left[aH + \frac{2aH_0}{2\sqrt{\Omega}}\frac{d\Omega}{dx} - \frac{aH_0}{4\Omega^{3/2}}\left(\frac{d\Omega}{dx}\right)^2 + \frac{aH_0}{2\sqrt{\Omega}}\frac{d^2\Omega}{dx^2}\right]$$

$$= 1 + \frac{1}{\Omega}\frac{d\Omega}{dx} - \frac{1}{4\Omega^2}\left(\frac{d\Omega}{dx}\right)^2 + \frac{1}{2\Omega}\frac{d^2\Omega}{dx^2}$$

During radiation domination $\Omega = \Omega_{r0}a^{-4} = \Omega_{r0}e^{-4x}$, so $\frac{d\Omega}{dx} = -4\Omega$, and $\frac{d^2\Omega}{dx^2} = 16\Omega$. Thus

$$\frac{1}{\mathcal{H}}\frac{d^2\mathcal{H}}{dx^2} = 1 - \frac{4\Omega}{\Omega} - \frac{16\Omega^2}{4\Omega^2} + \frac{16\Omega}{2\Omega} = 1 \tag{A.21}$$

Similarly, during matter domination $\Omega = \Omega_{m0}e^{-3x}$, so

$$\frac{1}{\mathcal{H}}\frac{d^2\mathcal{H}}{dx^2} = 1 - \frac{3\Omega}{\Omega} - \frac{9\Omega^2}{4\Omega^2} + \frac{9\Omega}{2\Omega} = \frac{1}{4} \tag{A.22}$$

And finally, during dark energy domination $\Omega = \Omega_{\Lambda0}$, so

$$\frac{1}{\mathcal{H}}\frac{d^2\mathcal{H}}{dx^2} = 1 \tag{A.23}$$

*Appendix A.4: $\eta(x)$ during radiation domination*

From equation (12) we can write

$$\frac{d\eta}{dx} = \frac{c}{aH} = \frac{c}{aH_0\sqrt{\Omega(a)}}, \tag{A.24}$$

where $\sqrt{\Omega(a)} = \frac{H}{H_0}$ is the same quantity as used previously. During radiation domination $\Omega(a) = a^{-4} = e^{-4x}$, so

$$\frac{d\eta}{dx} = \frac{c}{e^xH_0e^{-2x}} = \frac{c}{H_0}e^x, \tag{A.25}$$

which has solution

$$\eta(x) = \frac{c}{H_0}[e^x]_{-\infty}^x = \frac{c}{H_0}e^x = \frac{c}{e^xH_0e^{-2x}} = \frac{c}{e^xH_0\sqrt{\Omega}} = \frac{c}{\mathcal{H}} \tag{A.26}$$

We can derive a similar expression for $t(x)$ during radiation domination, from equation (13).

$$\frac{dt}{dx} = \frac{1}{H} = \frac{1}{H_0e^{-2x}} = \frac{1}{H_0}e^{2x}. \tag{A.27}$$

So

$$t(x) = \frac{1}{H_0}\left[e^{2x}\right]_{-\infty}^x = \frac{1}{2H_0}e^{2x} = \frac{1}{2H_0\sqrt{\Omega}} = \frac{1}{2H} \tag{A.28}$$

*Appendix A.5: m-r, m-$\Lambda$ equality and start of accelerated expansion*

The redshift corresponding to matter-radiation equality can be found in the following way

$$\Omega_{m0}(1+z)^3 = \Omega_{r0}(1+z)^4$$

$$\implies z_{eq} = \frac{\Omega_{m0}}{\Omega_{r0}} - 1.$$

And similarly for matter-dark energy equality

$$\Omega_{m0}(1+z)^3 = \Omega_{\Lambda0}$$

$$\implies z_{eq} = \left(\frac{\Omega_{\Lambda0}}{\Omega_{m0}}\right)^{1/3} - 1$$

The redshift at which accelerated expansion starts can be found from the second Friedmann equation:

$$\frac{\ddot{a}}{a} = -\frac{4\pi G}{3}\left(\rho + \frac{3p}{c^2}\right) \tag{A.29}$$

Close to the start of accelerated expansion $\rho = \rho_{m0}(1+z)^3 + \rho_{\Lambda0}$ and the pressure is only from dark energy, so $p = -\rho_{\Lambda0}c^2$. This gives

$$\frac{\ddot{a}}{a} = -\frac{4\pi G}{3}\left(\rho_{m0}(1+z)^3 + \rho_{\Lambda0} - 3\rho_{\Lambda0}\right) \tag{A.30}$$

The start of the accelerated epoch begins when $\ddot{a} = 0$, so when

$$\rho_{m0}(1 + z)^3 = 2\rho_{\Lambda 0}$$

$$\implies z = \left(\frac{2\rho_{\Lambda 0}}{\rho_{m0}}\right)^{1/3} - 1 = \left(\frac{2\Omega_{\Lambda 0}}{\Omega_{m0}}\right)^{1/3} - 1$$

## Appendix B: Recombination History

### Appendix B.1: Deriving explicit expression for $x_{H+}$, $x_{He+}$ and $x_{He++}$

Let the right hand sides of (31), (32) and (33) be $C_1$, $C_2$ and $C_3$ respectively. Then (33) can be rewritten into

$$x_{H+}(n_e + C_3) = C_3. \tag{B.1}$$

Such that

$$x_{H+} = \frac{C_3}{n_e + C_3}. \tag{B.2}$$

(32) can be written as

$$x_{He++} = \frac{C_2}{n_e}x_{He+}. \tag{B.3}$$

And (31) can be written as

$$\frac{n_e x_{He+}}{1 - x_{He+} - \frac{C_2}{n_e}x_{He+}} = C_1, \tag{B.4}$$

by inserting the expression for $x_{He++}$. By collecting terms with $x_{He+}$ and rearranging we get

$$x_{He+} = \frac{C_1}{n_e + C_1 + \frac{C_1 C_2}{n_e}}. \tag{B.5}$$

This in turn also gives an explicit expression for $x_{He++}$ in terms of the $C$'s and $n_e$.

## Appendix C: Power spectrum

### Appendix C.1: Changing cosmological parameters

When changing the cosmological parameters to see the effect on the power spectrum we want that effect to only be caused by the parameter we are changing. If we change $\Omega_{\Lambda 0}$ we want the power spectrum to only be changed due to $\Omega_{\Lambda 0}$, so that we can see how the density parameter of dark energy affects the power spectrum. But that will not be the case if we change $\Omega_{\Lambda 0}$ while keeping $h$ constant. Then $\Omega_{m0}$ will also change, since $\Omega_{m0} + \Omega_{\Lambda 0} = 1$. We will thus achieve the wanted effect on the power spectrum due to the change in $\Omega_{\Lambda 0}$, but we also get an additional unwanted effect of the change in $\Omega_{m0}$ (This discussion parallels that in section 8.7 of Dodelson (2011)). This would also cause $\Omega_{m0}h^2$ to change, and since this determines when matter-radiation equality occurred, it will also cause a change in the power spectrum. But this is readily fixed by instead changing for example $\Omega_{\Lambda 0}$ and keeping $\Omega_{m0}h^2$ fixed. The changes we will perform are

- Change $\Omega_{\Lambda 0}$ and keep $\Omega_{m0}h^2$ constant
- Change $\Omega_{m0}$ and keep $\Omega_{\Lambda 0}h^2$ and $\Omega_{b0}h^2$ constant
- Change $\Omega_{b0}$ and keep $\Omega_{m0}$ (and thus also $\Omega_{\Lambda 0}$) constant

and we now discuss how this is achieved. In the following we neglect $\Omega_{\gamma 0}$, because it is so small compared to the other density parameters. We just want to see how the power spectrum changes visually, so this approximation is good enough.

### Appendix C.1.1: Change $\Omega_{\Lambda 0}$ and keep $\Omega_{m0}h^2$ constant

We enforce

$$\Omega_{\Lambda 0} + \Omega_{b0} + \Omega_{CDM0} = 1 \tag{C.1}$$

and that

$$\Omega_{b0}h^2 = x_b \tag{C.2}$$
$$\Omega_{CDM0}h^2 = x_{CDM} \tag{C.3}$$

where $x_b$ and $x_{CDM}$ are constant. These $x$'s are first calculated for the fiducial model. Now divide (C.2) and (C.3) by $h^2$ and insert into (C.1). After some algebra we get

$$h = \sqrt{\frac{x_b + x_{CDM}}{1 - \Omega_{\Lambda 0}}} \tag{C.4}$$

This $h$ can then be inserted into (C.2) and (C.3) to find the new values of $\Omega_{b0}$ and $\Omega_{CDM0}$.

### Appendix C.1.2: Change $\Omega_{m0}$ and keep $\Omega_{\Lambda 0}h^2$ and $\Omega_{b0}h^2$ constant

The procedure here is almost completely the same as when changing $\Omega_{\Lambda 0}$. We now start with the requirement that $\Omega_{m0} + \Omega_{\Lambda 0} = 1$ and enforce $\Omega_{\Lambda 0}h^2 = x_\Lambda$. In analogy with (C.4) we get

$$h = \sqrt{\frac{x_\Lambda}{1 - \Omega_{m0}}} \tag{C.5}$$

The only difference is that now we do not require that $\Omega_{CDM0}h^2$ is constant, only $\Omega_{b0}h^2$. So

$$\Omega_{b0} = \frac{x_b}{h^2} \tag{C.6}$$
$$\Omega_{CDM0} = \Omega_{m0} - \Omega_{b0} \tag{C.7}$$

### Appendix C.1.3: Change $\Omega_{b0}$ and keep $\Omega_{m0}$ (and thus also $\Omega_{\Lambda 0}$) constant

This is the simplest of the three. We simply calculate $\Omega_{m0} = \Omega_{b0} + \Omega_{CDM0}$ for the fiducial model. Then we change $\Omega_{b0}$ and $\Omega_{CDM0}$ is then given by $\Omega_{m0} - \Omega_{b0}$.